



**HAL**  
open science

# A technique of flux reconstruction at the interfaces of nonconforming grids for aeroacoustic simulations

Sophie Le Bras, Hugues Deniau, Christophe Bogey

► **To cite this version:**

Sophie Le Bras, Hugues Deniau, Christophe Bogey. A technique of flux reconstruction at the interfaces of nonconforming grids for aeroacoustic simulations. *International Journal for Numerical Methods in Fluids*, 2019, 91 (12), pp.587-614. 10.1002/fld.4767 . hal-02351079

**HAL Id: hal-02351079**

**<https://hal.science/hal-02351079v1>**

Submitted on 24 Nov 2020

**HAL** is a multi-disciplinary open access archive for the deposit and dissemination of scientific research documents, whether they are published or not. The documents may come from teaching and research institutions in France or abroad, or from public or private research centers.

L'archive ouverte pluridisciplinaire **HAL**, est destinée au dépôt et à la diffusion de documents scientifiques de niveau recherche, publiés ou non, émanant des établissements d'enseignement et de recherche français ou étrangers, des laboratoires publics ou privés.

# A technique of flux reconstruction at the interfaces of non-conforming grids for aeroacoustic simulations

S. Le Bras<sup>1,2\*</sup>, H. Deniau<sup>3</sup> and C. Bogey<sup>4</sup>

<sup>1</sup> *Centre Européen de Recherche et de Formation Avancée en Calcul Scientifique, 31057 Toulouse, France.*

<sup>2</sup> *Siemens Industry Software N.V., 3001 Leuven, Belgium.*

<sup>3</sup> *ONERA, French Aerospace Lab, 31000 Toulouse, France.*

<sup>4</sup> *Univ Lyon, Ecole Centrale de Lyon, INSA Lyon, Université Claude Bernard Lyon I, CNRS, Laboratoire de Mécanique des Fluides et d'Acoustique, UMR 5509, F-69134, Ecully, France.*

## SUMMARY

A flux reconstruction technique is presented in order to perform aeroacoustic computations using implicit high-order spatial schemes on multiblock structured grids with non-conforming interfaces. The use of such grids, with mesh spacing discontinuities across the block interfaces, eases local mesh refinements, simplifies the mesh generation process, and thus facilitates the computation of turbulent flows. In this work, the spatial discretization consists of sixth-order finite-volume implicit schemes with low-dispersion and low-dissipation properties. The flux reconstruction is based on the combination of non-centered schemes with local interpolations to define ghost cells and compute flux values at the grid interfaces. The flow variables in the ghost cells are calculated from the flow field in the grid cells using a meshless interpolation with radial basis functions. In this study, the flux reconstruction is applied to both plane and curved non-conforming interfaces. The performance of the method is first evaluated by performing two-dimensional simulations of the propagation of an acoustic pulse and of the convection of a vortex on Cartesian and wavy grids. No significant spurious noise is produced at the grid interfaces. The applicability of the flux reconstruction to a 3-D computation is then demonstrated by simulating a jet at a Mach number of 0.9 and a diameter-based Reynolds number of  $4 \times 10^5$  on a Cartesian grid. The non-conforming grid interface located downstream of the jet potential core does not appreciably affect the flow development and the jet sound field, while reducing the number of mesh points by a factor of approximately two.

Copyright © 2018 John Wiley & Sons, Ltd.

Received ...

**KEY WORDS:** non-conforming grids, structured grids, high-order schemes, finite volumes, meshless interpolation, aeroacoustics

## 1. INTRODUCTION

For flows at high Reynolds numbers, the direct computation of the aerodynamic noise from the Navier-Stokes equations requires accurate numerical methods in order to properly compute both the

\*Correspondence to: Sophie Le Bras, Siemens Industry Software N.V., Interleuvenlaan 68, 3001 Leuven, Belgium.  
E-mail: sophie.le\_bras@siemens.com

14 small turbulent motions and the low-frequency sound waves in the radiated pressure field [1–3]. In  
 15 order to meet these requirements, in addition to high-order discretization schemes, locally refined  
 16 meshes are needed in order to capture the turbulent eddies generating noise [4].

17 For aeroacoustic simulations performed on multiblock structured grids, the computational domain  
 18 is usually divided into subdomains composed of conforming grids characterized by a full point-  
 19 matching distribution at the block interface, as shown in Fig. 1(a). Difficulties in performing high-  
 20 fidelity computations with such grids arise when the geometries are complex. Such geometries  
 21 must be included in the numerical simulations in order to faithfully reproduce the conditions of the  
 22 experiments [5, 6]. In this context, high-quality structured meshes with conforming interfaces are in  
 23 many cases almost impossible to generate [7]. For instance, for high-speed flows exhausting from  
 24 turbofan jet engines or developing on aircraft wings [8], extremely fine grids are required to resolve  
 25 the flow in the boundary layers and the wakes. Using conforming grids, local mesh refinements  
 26 can be found in all the computational domain, leading to an excessive number of mesh points as  
 27 well as to the generation of extremely small cells in out of interest areas. Obviously, this increases  
 28 the computational cost of the simulation. In addition, using an explicit time discretization scheme,  
 29 the presence of very small mesh cells imposes severe constraints on the time step so that the CFL  
 restriction is verified [3].

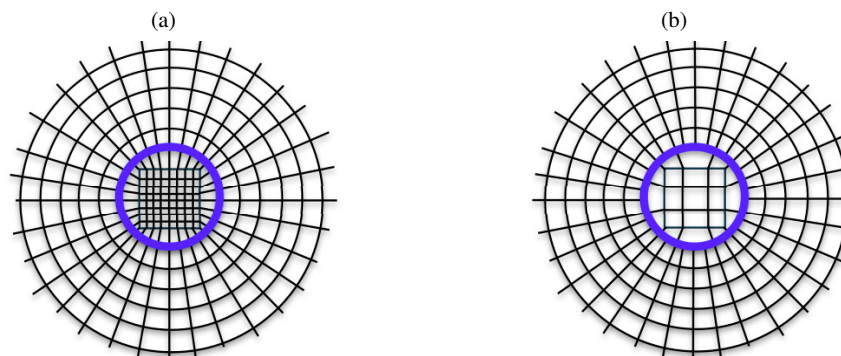


Figure 1. Representation of 2-D meshes with (a) conforming and (b) non-conforming grid interfaces in blue.

30 In order to perform aeroacoustic simulations of high-Reynolds-number flows at a reasonable  
 32 computational cost, the use of non-conforming grids [9] without overlapping is attractive. Such  
 33 meshes exhibit discontinuities of the grid lines across the block interface. This is the case of  
 34 Fig. 1(b), providing an example of a non-conforming mesh with discontinuous grid spacings in the  
 35 azimuthal direction at the block interface in blue. Using such a mesh for instance, the refinement at  
 36 the center of the grid in Fig. 1(a) can be avoided. The size of the smallest cells and thus the time  
 37 step are therefore chosen such that the acoustic sources are well-discretized. In addition, the use  
 38 of non-conforming grids simplifies the grid generation process since the mesh blocks composing  
 39 the computational domain can be created independently and then easily assembled. In return, in  
 40 order to obtain high-fidelity numerical results using non-conforming grids, an accurate spatial  
 41 discretization at the grid interfaces is required. Indeed, as the grid spacing is discontinuous at the  
 42 block interface, the spatial discretization schemes cannot usually be applied close to the interface  
 43 and their formulations have to be modified.

44 In computational aeroacoustics, the spatial discretization can be carried out using high-order  
 45 low-dissipation and low-dispersion schemes, amongst which the dispersion-relation-preserving

46 schemes [10], the optimized explicit schemes in the Fourier space [2], or the implicit schemes [11,  
47 12]. In this study, the spatial discretization consists of the sixth-order finite-volume implicit scheme  
48 of Fosso *et al.* [12] in combination with the sixth-order implicit selective filter of Visbal and  
49 Gaitonde [13]. Implicit schemes are particularly attractive in order to reach a high-order spectral  
50 accuracy using a smaller number of grid points compared to explicit schemes. However, in the  
51 context of parallel computations, the flow equations are generally solved locally in each subdomain  
52 of the multiblock grid. As a consequence, the implicit centered schemes cannot be applied at the  
53 mesh block interfaces. Therefore, in a previous study [12], a technique of flux reconstruction at the  
54 interface of conforming grids has been developed. Based on the application of non-centered spatial  
55 schemes at the block interface and the use of ghost cells, the technique allowed us to successfully  
56 perform massively parallel aerodynamic and aeroacoustic computations of jet flows [14–17].

57 In the present study, a flux reconstruction technique for the interface of non-conforming grids  
58 is proposed. The technique, derived from the method developed for conforming grids [12], is  
59 based on the application of non-centered schemes at the grid interface. Due to the mesh line  
60 discontinuities at the grid interface, an additional step consisting in reconstructing ghost cells is  
61 required. The flow variables in the ghost cells are computed using a local interpolation technique,  
62 based on a meshless method involving Radial Basis Functions (RBF) [9, 18]. Meshless interpolations  
63 are useful in order to alleviate the difficulties caused by the loss of the mesh topology at the  
64 interfaces of non-conforming grids. Indeed, since meshless interpolations are performed from  
65 arbitrarily scattered spatial data without any geometrical information, computational overheads  
66 due to topology reconstructions are avoided. Originally developed by the authors for plane non-  
67 conforming grid interfaces [19], the technique of flux reconstruction is extended to curved interfaces  
68 in this study. In comparison with the preliminary results presented in [19], the properties of the  
69 RBF interpolation are examined in 1-D in the wavenumber space, and the performance of the flux  
70 reconstruction is further assessed by simulating in 2-D the convection of a vortex on wavy grids  
71 and the propagation of an acoustic pulse. In addition, the application of the technique to a three-  
72 dimensional turbulent jet flow is presented.

73 The present paper is organized as follows. In a first section, the high-order finite-volume approach  
74 used in this study and the flux reconstruction method for conforming interfaces are described.  
75 In section 2, the reconstruction technique developed at the interface of plane and curved non-  
76 conforming grids is presented. In section 3, the properties of the RBF interpolations are examined  
77 in 1-D in the wavenumber space. In section 4, the accuracy of the flux reconstruction is evaluated  
78 by simulating a two-dimensional acoustic pulse propagating through a non-conforming interface. In  
79 section 5, the simulations of two-dimensional vortex convection for Cartesian and wavy grids with  
80 different spatial resolutions are presented. In particular, the advantages of using RBF interpolations  
81 for the reconstruction and the choice of the interpolation parameters are discussed. Finally, the  
82 application of the technique to a 3-D turbulent jet flow is presented, using a non-conforming grid  
83 downstream of the jet potential core. The reduction in the number of mesh points obtained using a  
84 non-conforming grid is evaluated. The effects of the presence of a non-conforming interface on the  
85 sound field radiated by the jet are examined.

## 2. FLUX RECONSTRUCTION TECHNIQUE FOR CONFORMING GRIDS

### 86 2.1. Governing equations

87 In this study, the 3-D compressible Navier-Stokes equations are solved. Using Cartesian coordinates,  
88 they can be written as:

$$\frac{\partial \mathbf{W}}{\partial t} + \frac{\partial \mathbf{E}_c}{\partial x} + \frac{\partial \mathbf{F}_c}{\partial y} + \frac{\partial \mathbf{G}_c}{\partial z} - \frac{\partial \mathbf{E}_d}{\partial x} - \frac{\partial \mathbf{F}_d}{\partial y} - \frac{\partial \mathbf{G}_d}{\partial z} = 0 \quad (1)$$

89 where  $(\mathbf{E}_c, \mathbf{F}_c, \mathbf{G}_c)$  are the convective fluxes,  $(\mathbf{E}_d, \mathbf{F}_d, \mathbf{G}_d)$  are the diffusive fluxes,  
90  $\mathbf{W} = (\rho, \rho u, \rho v, \rho w, \rho e)^t$  is the vector of the conservative variables,  $\rho$  is the density,  $(u, v, w)$  are the  
91 velocity components, and  $\rho e$  is the total energy. For a perfect gas, the total energy  $\rho e$  is given by:

$$\rho e = \frac{p}{\gamma - 1} + \frac{1}{2} \rho (u^2 + v^2 + w^2) \quad (2)$$

92 where  $p$  is the static pressure and  $\gamma$  is the specific heat ratio. The convective fluxes write as:

$$\begin{cases} \mathbf{E}_c = (\rho u, \rho u^2 + p, \rho uv, \rho uw, (\rho e + p)u)^t \\ \mathbf{F}_c = (\rho v, \rho uv, \rho v^2 + p, \rho vw, (\rho e + p)v)^t \\ \mathbf{G}_c = (\rho w, \rho uw, \rho vw, \rho w^2 + p, (\rho e + p)w)^t \end{cases} \quad (3)$$

93 and the diffusive fluxes as:

$$\begin{cases} \mathbf{E}_d = (0, \tau_{11}, \tau_{12}, \tau_{13}, \tau_{11}u + \tau_{12}v + \tau_{13}w + H_1)^t \\ \mathbf{F}_d = (0, \tau_{21}, \tau_{22}, \tau_{23}, \tau_{21}u + \tau_{22}v + \tau_{23}w + H_2)^t \\ \mathbf{G}_d = (0, \tau_{31}, \tau_{32}, \tau_{33}, \tau_{31}u + \tau_{32}v + \tau_{33}w + H_3)^t \end{cases} \quad (4)$$

94 where  $\mathbf{H} = (H_1, H_2, H_3)^t$  is the heat flux vector,  $\tau_{ij} = 2\mu S_{ij}$  is the viscous stress tensor,  $\mu$  is the  
95 dynamic molecular viscosity computed from Sutherland's law, and  $S_{ij}$  is the deformation stress  
96 tensor:

$$S_{ij} = \frac{1}{2} \left( \frac{\partial u_i}{\partial x_j} + \frac{\partial u_j}{\partial x_i} - \frac{2}{3} \frac{\partial u_k}{\partial x_k} \delta_{i,j} \right) \quad (5)$$

97 The heat flux vector  $\mathbf{H}$  is computed from Fourier's law, yielding:

$$\mathbf{H} = -\lambda \nabla T \quad (6)$$

98 where  $\nabla T$  is the temperature gradient,  $\lambda = C_p \mu / Pr$  is the thermal conductivity,  $C_p$  is the specific  
99 heat at constant pressure, and  $Pr$  is the Prandtl number.

### 100 2.2. High-order finite-volume approach

101 The computations are performed using the finite-volume multi-block structured solver *elsA* [20],  
102 allowing us to perform Direct Numerical Simulations (DNS) or Large-Eddy Simulations (LES). In  
103 a finite-volume approach, the integral form of the Navier-Stokes equation (1) is solved at a discrete  
104 level. For this purpose, the computational domain is divided into non-overlapping control volumes  
105  $\Omega_i$ , where  $i$  is the volume index. Integrating Eq. (1) over the elementary volumes  $\Omega_i$  and using the

106 divergence theorem lead to:

$$|\Omega_i| \frac{d\mathbf{U}_i}{dt} + \int_{\partial\Omega_i} (\mathbf{E}_c + \mathbf{F}_c + \mathbf{G}_c) \cdot \mathbf{n} \, dS + \int_{\partial\Omega_i} (\mathbf{E}_d + \mathbf{F}_d + \mathbf{G}_d) \cdot \mathbf{n} \, dS = 0 \quad (7)$$

107 where  $\mathbf{n} = (n_x, n_y, n_z)$  is the outgoing unitary normal of  $\Omega_i$ ,  $\partial\Omega_i$  represents the faces of  $\Omega_i$  and  $\mathbf{U}_i$   
 108 is the mean value of  $\mathbf{W}$  in the volume  $\Omega_i$  such as:

$$\mathbf{U}_i = \frac{1}{|\Omega_i|} \int_{\Omega_i} \mathbf{W} \, dV \quad (8)$$

109 In the *elsA* solver, the diffusive fluxes in Eq. (7) are calculated from the gradient  $\nabla\mathbf{U}$  estimated at  
 110 the cell interfaces using a 2nd-order method [21]. For clarity, in the following, only the convective  
 111 fluxes are presented in the equations. Following Fosso *et al.* [12] and supposing that the volume  $\Omega_i$   
 112 is an hexahedron, the normal  $\mathbf{n}$  is constant along the interface, and the integral of the convective  
 113 fluxes in Eq. (7) can be approximated as:

$$\int_{\partial\Omega_i} (\mathbf{E}_c + \mathbf{F}_c + \mathbf{G}_c) \cdot \mathbf{n} \, dS \simeq |\partial\Omega_i| \left( \mathbf{E}_c(\tilde{\mathbf{U}}_{\partial\Omega_i})n_x + \mathbf{F}_c(\tilde{\mathbf{U}}_{\partial\Omega_i})n_y + \mathbf{G}_c(\tilde{\mathbf{U}}_{\partial\Omega_i})n_z \right) \quad (9)$$

114 where  $\tilde{\mathbf{U}}_{\partial\Omega_i}$  is the averaged value of the variable vector  $\mathbf{W}$  at the cell interface  $\partial\Omega_i$ :

$$\tilde{\mathbf{U}}_{\partial\Omega_i} = \frac{1}{|\partial\Omega_i|} \int_{\partial\Omega_i} \mathbf{W} \, dS \quad (10)$$

115 The convective fluxes are thus computed from the interface-averaged values  $\tilde{\mathbf{U}}$  of the flow variables.  
 116 In order to obtain a high-order calculation of the convective fluxes derivatives, a high-order  
 117 interpolation of vector  $\tilde{\mathbf{U}}$  is performed from the cell-averaged values  $\mathbf{U}$ . Considering the one-  
 118 dimensional computational domain of Fig. 2, the interpolated vector  $\tilde{\mathbf{U}}$  at the interface  $i + 1/2$  is  
 119 obtained by solving the implicit scheme:

$$\alpha_{i+1/2} \tilde{\mathbf{U}}_{i-1/2} + \tilde{\mathbf{U}}_{i+1/2} + \beta_{i+1/2} \tilde{\mathbf{U}}_{i+3/2} = \sum_{l=-1}^2 a_l \mathbf{U}_{i+l} \quad (11)$$

120 where  $\alpha_{i+1/2}$ ,  $\beta_{i+1/2}$  and  $a_l$  are the scheme coefficients which are obtained from a 5th-order Taylor  
 121 series [12]. This scheme correctly resolves the wavelengths discretized by at least 5 points [14].  
 122 Note that despite the use of approximation (9) which is formally only second-order accurate, Fosso  
 123 *et al.* [12] demonstrated that the numerical scheme (11) is equivalent to Lele's 6th-order finite-  
 difference scheme [11] for a uniform Cartesian mesh.

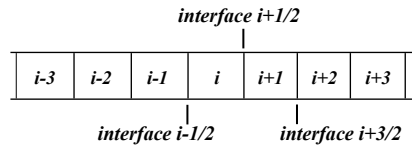


Figure 2. Representation of a one-dimensional computational domain.

124

125 In order to ensure the stability of the centered scheme (11), the 6th-order compact filter of Visbal  
 126 and Gaitonde [13] is applied to the flow variables. The filtered values, denoted  $\hat{\mathbf{U}}$ , are estimated

127 from the values of  $\mathbf{U}$  as:

$$\alpha_f \widehat{\mathbf{U}}_{i-1} + \widehat{\mathbf{U}}_i + \alpha_f \widehat{\mathbf{U}}_{i+1} = \sum_{l=0}^3 \frac{\gamma_l}{2} (\mathbf{U}_{i+l} + \mathbf{U}_{i-l}) \quad (12)$$

128 where  $\alpha_f = 0.47$ , and  $\gamma_l$  are the filter coefficients [13]. The filter is employed on a uniformly  
 129 spaced grid thanks to a coordinate transform. For LES computations, the filter also plays the role  
 130 of a subgrid-scale model, relaxing turbulent energy at high frequencies [22–24]. Time integration  
 131 is performed by applying a low-storage 6-stage Runge Kutta algorithm [2]. Radiation boundary  
 132 conditions, Navier-Stokes characteristic boundary conditions, and sponge zones are used in order  
 133 to avoid significant acoustic reflections at the mesh boundaries. A more detailed description of the  
 134 numerical algorithm is given in Fosso *et al.* [14].

### 135 2.3. Reconstruction for conforming grid interfaces

136 2.3.1. Numerical scheme At the mesh-block interfaces, the implicit centered scheme (11) used in  
 137 the computation of the convective fluxes cannot be applied. Thus, in a previous study [12], a flux  
 138 reconstruction technique has been proposed at the interfaces of conforming grids. It is presented in  
 139 the following by considering a two-dimensional computational domain composed of two blocks L  
 and R separated by a conforming interface, as shown in Fig. 3.

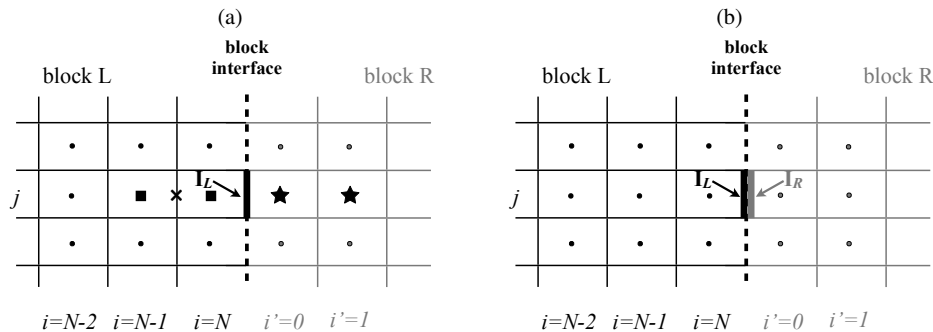


Figure 3. Flux reconstruction for conforming grids: (a) step 1: computation of the flow variables at the interface  $\mathbf{I}_L$  using a scheme involving two cells (squares) and an interface (cross) of block L and two ghost cells (stars) of block R, (b) step 2: flux computation from the flow variables at the interfaces  $\mathbf{I}_L$  and  $\mathbf{I}_R$ , using a Riemann solver.

140

141 The reconstruction technique consists of two steps. In the first step, the flow variables  $\widetilde{\mathbf{U}}$  at the grid  
 142 interface in blocks L and R are determined using upwind schemes. More precisely, in block L, as  
 143 illustrated in Fig. 3(a), the vector  $\widetilde{\mathbf{U}}_L$  at the interface  $I_L$  is computed using a non-centered scheme  
 144 involving the flow variables in cells of blocks L and R such as:

$$\alpha' \widetilde{\mathbf{U}}_{i=N-1/2,j} + \widetilde{\mathbf{U}}_L = \underbrace{a'_0 \mathbf{U}_{i=N-1,j} + a'_1 \mathbf{U}_{i=N,j}}_{\text{cells of block L}} + \underbrace{a'_2 \mathbf{U}_{i'=0,j} + a'_3 \mathbf{U}_{i'=1,j}}_{\text{cells of block R}} \quad (13)$$

145 where  $\alpha'$  and  $a'_i$  are the scheme coefficients determined using Taylor series. For block L, the values  
 146 of  $\mathbf{U}$  in the cells  $(i' = 0, j)$  and  $(i' = 1, j)$  of block R are a priori not known. These cells are thus  
 147 referred to as ghost cells for block L in the following. The values of  $\mathbf{U}$  in the ghost cells are obtained  
 148 thanks to data exchanges between the blocks at each time iteration of the simulation. Symmetrically,

149 in block R, the vector  $\tilde{\mathbf{U}}_R$  at the interface  $I_R$  in Fig. 3(b) is determined from the upwind scheme:

$$\tilde{\mathbf{U}}_R + \beta'' \tilde{\mathbf{U}}_{i'=1/2,j} = \underbrace{a_0'' \mathbf{U}_{i=N-1,j} + a_1'' \mathbf{U}_{i=N,j}}_{\text{cells of block L}} + \underbrace{a_2'' \mathbf{U}_{i'=0,j} + a_3'' \mathbf{U}_{i'=1,j}}_{\text{cells of block R}} \quad (14)$$

150 where  $\beta''$  and  $a_i''$  are the scheme coefficients. The values of  $\tilde{\mathbf{U}}_L$  and  $\tilde{\mathbf{U}}_R$  are usually not identical,  
 151 since they are determined from two different upwind schemes (13) and (14). Therefore, in a second  
 152 step, a Riemann problem [25] is solved in order to ensure the unicity of the flux, hence the scheme  
 153 conservativity, at the block interface.

154 2.3.2. *Selective filter* In the vicinity of conforming grid interfaces, as for the centered scheme (11),  
 155 the 7-point centered filter (12) cannot be applied, and its formulation has to be modified. However,  
 156 previous studies [26] demonstrated that the change of the filter formulation at the grid interface is  
 157 likely to significantly decrease the accuracy of the filtering process and generate spurious noise.  
 158 Therefore, in order to still apply the centered filter (12) at the grid interface, Fosso [26] proposed to  
 159 artificially extend the size of the mesh blocks using ghost cells, and to modify the filter formulation  
 160 in the ghost cell regions exclusively. In practice, according to the notations of Fig. 4, in order to  
 161 change the filter formulation as far as possible from the interface, the block L is extended using  
 162 five ghost cells represented by stars. These cells correspond to the cells of block R indexed by  
 163  $i' = 0, 1, 2, 3, 4$ . Consequently, in block L, the centered filter (12) on 7 points can be applied in cells  
 164  $i = \dots, N - 1, N$  and in the ghost cell ( $i' = 0, j$ ). Finally, a non-centered filter is used in order to  
 165 determine the value of  $\hat{\mathbf{U}}$  in the ghost cell ( $i' = 1, j$ ) in grey in Fig. 4:

$$\alpha_f \hat{\mathbf{U}}_{i'=0,j} + \hat{\mathbf{U}}_{i'=1,j} = \sum_{k=2}^3 \frac{\gamma_k}{2} \mathbf{U}_{i=N-k+2,j} + \frac{\gamma_1}{2} \mathbf{U}_{i'=0,j} + \gamma_0 \mathbf{U}_{i'=1,j} + \sum_{k=1}^3 \frac{\gamma_k}{2} \mathbf{U}_{i'=k+1,j} - \alpha_f \mathbf{U}_{i'=2,j} \quad (15)$$

166 The flux reconstruction for conforming grids presented in this section has been successfully applied  
 to massively parallel aeroacoustic simulations of jet flows at high Reynolds numbers [14, 15, 17].

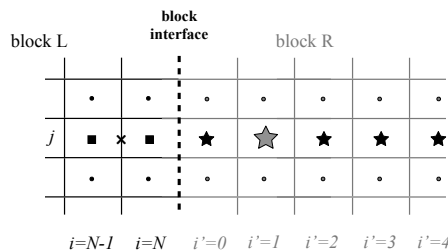


Figure 4. Filter application in block L in the vicinity of a conforming grid interface: the flow variables in the ghost cell  $i' = 1$  in grey are filtered using grid cells of block L (squares) and block R (stars).

167

### 3. FLUX RECONSTRUCTION TECHNIQUE FOR NON-CONFORMING GRIDS

168 In this section, the reconstruction presented above for conforming grids is extended to the cases of  
 169 plane and curved non-conforming meshes.



### 170 3.1. Plane interfaces

171 In the case of a non-conforming grid interface, as illustrated in Fig. 5, the flux reconstruction  
 172 technique described in section 2.3 cannot be used. Indeed, for such grids, as the mesh lines are  
 173 discontinuous across the block interface, the ghost cells represented by stars in Fig. 4 are not defined  
 174 anymore. Therefore, the upwind schemes (13) (14) and the filter (15) cannot be applied. In this work,  
 175 a new flux reconstruction is thus proposed at the non-conforming interfaces. It consists in using non-  
 176 centered schemes and meshless interpolations in order to define the flow variables in ghost cells and  
 177 at the grid interface. In this section, the flux reconstruction is presented for the plane grid interface  
 178 displayed in Fig. 5, considering block L as the current block.

179 3.1.1. *Numerical scheme* In order to compute the flux at the interface  $I_L$  in block L, the key idea  
 180 is to make possible the application of the schemes (13) and (14) thanks to the reconstruction of the  
 181 flow variables in ghost cells. For this purpose, a methodology, composed of four steps depicted in  
 182 Fig. 5, is presented. In step 1, two ghost cells, represented in grey in Fig. 5(a), are defined. The  
 183 centers of these cells, depicted by stars, are located at the intersection between the mesh lines  $i' = 0$   
 184 and  $i' = 1$  and the straight line passing by the centers of the cells  $(i = N - 1, j)$  and  $(i = N, j)$ .  
 185 The values of the flow variables  $\mathbf{U}$  in the ghost cells are determined from the values of  $\mathbf{U}$  in  
 186 the cells of block R using a meshless interpolation. The interpolation technique is presented in  
 187 section 3.1.3. In step 2, illustrated in Fig. 5(b), the upwind scheme (13) can be applied to compute  
 188 the flow vector  $\tilde{\mathbf{U}}_L$  at the interface  $I_L$  of block L. In step 3, symmetrically with what was done in  
 189 steps 1 and 2 for block L, ghost cells are defined in block R and the scheme (14) is employed to  
 190 determine the vector  $\tilde{\mathbf{U}}$  at the interfaces  $(\dots, I_{R,j'}, I_{R,j'+1}, \dots)$  in grey in Fig. 5(c). Finally, in step  
 191 4, a ghost interface  $I'_L$ , identical geometrically to  $I_L$ , is defined in block R, as shown in Fig. 5(d).  
 192 The variable vector  $\tilde{\mathbf{U}}'_L$  at the interface  $I'_L$  is interpolated from the values  $\tilde{\mathbf{U}}$  obtained in step 3.  
 193 This second interpolation method is also described in section 3.1.3. Even if the interfaces  $I'_L$  and  $I_L$   
 194 are geometrically identical, the values of  $\tilde{\mathbf{U}}$  at these two interfaces differ since they are computed  
 195 from different schemes and interpolations. Therefore, the convective flux at the block interface is  
 196 determined from the values of  $\tilde{\mathbf{U}}_L$  and  $\tilde{\mathbf{U}}'_L$  by resolving a Riemann flux problem [25].

197 3.1.2. *Selective filter* Five ghost cells are necessary in order to apply the non-centered filter (15)  
 198 near the block interface. For conforming grids, as explained in section 2.3, the flow variables  
 199 in the ghost cells are directly obtained thanks to data exchanges between blocks. However,  
 200 for non-conforming grids, these variables first need to be interpolated before being exchanged.  
 201 Consequently, using five ghost cells results in an extra computational cost compared to conforming  
 202 grids, which led us to only consider two ghost cells. The application of the filter close to the non-  
 203 conforming interface of block L is illustrated in Fig. 6. The cells and ghost cells of block L involved  
 204 in the filtering are represented by squares and stars, respectively. As shown in Fig. 6(a), using two  
 205 ghost cells, the 7-point centered filter (12) can be applied as far as point  $(i = N - 1, j)$  in block L.  
 206 At the cell  $(i = N, j)$  adjacent to the block interface, in grey in Fig. 6(b), the filtered field  $\hat{\mathbf{U}}_{i=N,j}$   
 207 is computed from the upwind formulation:

$$\alpha_f \hat{\mathbf{U}}_{i=N-1,j} + \hat{\mathbf{U}}_{i=N,j} + \alpha_f \hat{\mathbf{U}}_{i'=0,j} = \sum_{k=0}^4 \gamma'_k \mathbf{U}_{N-4+k,j} + \gamma'_5 \mathbf{U}_{i'=0,j} + \gamma'_6 \mathbf{U}_{i'=1,j} \quad (16)$$

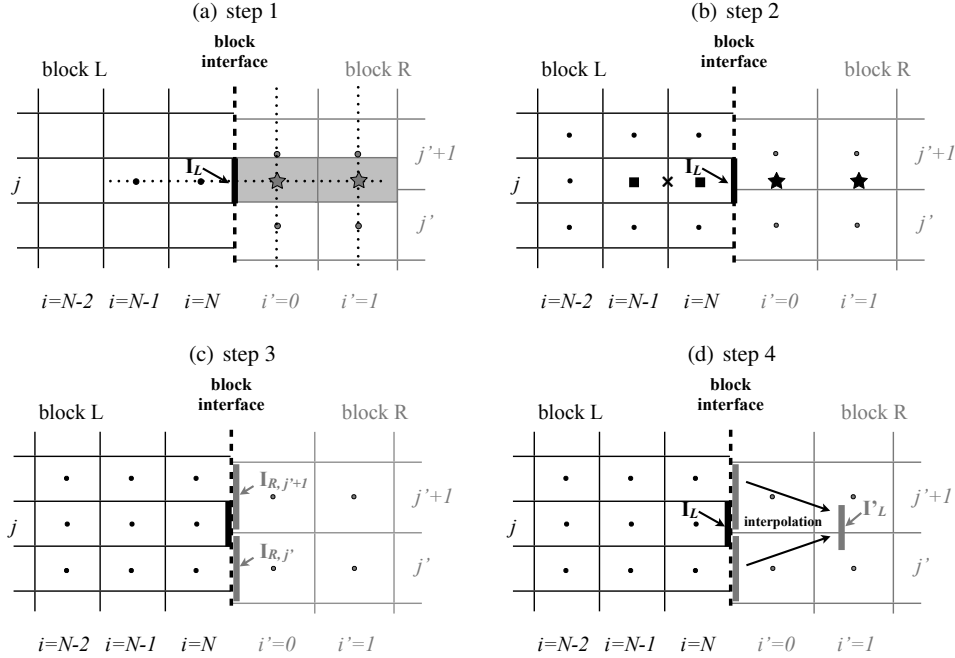


Figure 5. Flux reconstruction for non-conforming grids at the interface  $I_L$  in block L: (a) step 1: definition of two ghost cells (stars), (b) step 2: computation of the flow variables at the interface  $I_L$  using a non-centered scheme involving an interface (cross) and two cells (squares) of block L, and two ghost cells (stars), (c) step 3: computation of the flow variables at the interfaces in grey, applying steps 1 and 2 in block R, (d) step 4: interpolation of the flow variables at the ghost interface  $I'_L$  using the data computed in step 3, and computation of the resulting flux at the block interface using a Riemann solver.

208 Finally, the flow variables in the ghost cells  $(i' = 0, j)$  and  $(i' = 1, j)$  are filtered using non-centered  
 209 schemes on 7 points, as illustrated in Fig. 6(c) and 6(d), yielding:

$$\begin{cases} \alpha_f \widehat{U}_{i=N,j} + \widehat{U}_{i'=0,j} + \alpha_f \widehat{U}_{i'=1,j} = \sum_{k=0}^4 \gamma_k'' U_{N-4+k,j} + \gamma_5'' U_{i'=0,j} + \gamma_6'' U_{i'=1,j} \\ \alpha_f \widehat{U}_{i'=0,j} + \widehat{U}_{i'=1,j} = \sum_{k=0}^4 \gamma_k''' U_{N-4+k,j} + \gamma_5''' U_{i'=0,j} + \gamma_6''' U_{i'=1,j} \end{cases} \quad (17)$$

210 where  $\alpha_f = 0.47$ , and  $\gamma_k'$ ,  $\gamma_k''$  and  $\gamma_k'''$  are the non-centered filter coefficients [27].

211 **3.1.3. Interpolation techniques** In the flux reconstruction for non-conforming grids, interpolations  
 212 are performed in order to compute the flow variables  $\mathbf{U}$  in two ghost cells and the values of  $\tilde{\mathbf{U}}$  at  
 213 the grid interface. As presented in section 3.1.1, in block L, the interpolations are carried out using  
 214 values of  $\mathbf{U}$  and  $\tilde{\mathbf{U}}$  in block R. In practice, block R can be divided into subdomains with a loss of  
 215 topology information between the domains. Therefore, in this study, meshless interpolations based  
 216 on Radial Basis Functions (RBF) are employed.

217 First, the interpolation technique is described for the calculation of a component  $u$  of the vector  
 218  $\mathbf{U}$  in the ghost cell located at  $i' = 0$  in Fig. 5(a). The calculation is performed using the value of  $u$   
 219 known in  $n_v$  cells of block R surrounding the ghost cell. These  $n_v$  cells are located along the line  
 220  $i' = 0$  for a 2-D mesh, in the plane  $i' = 0$  for a 3-D straight mesh. The RBF approximation  $u_{\text{RBF}}$  of

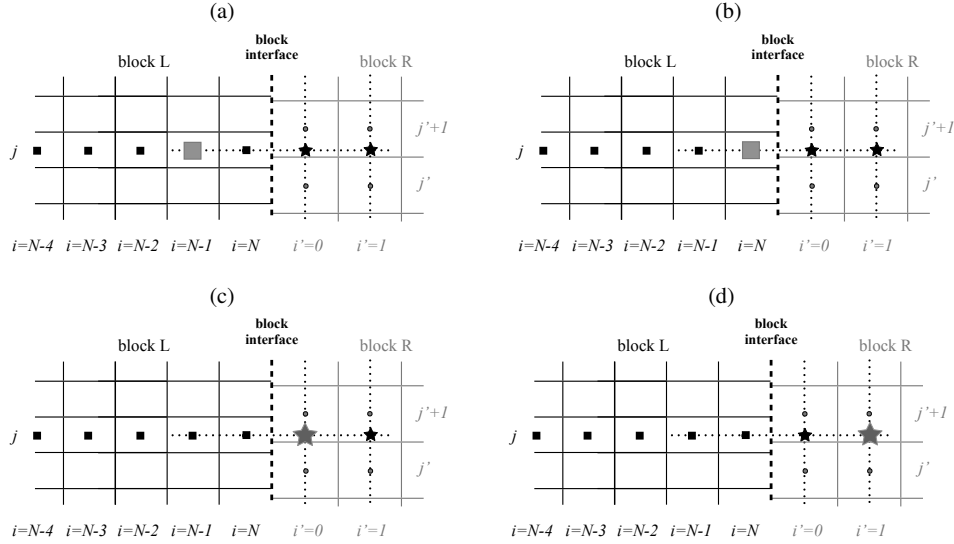


Figure 6. Filtering at the non-conforming grid interface in block L. Cells in block L (squares) and ghost cells in block R (stars) used in the filter scheme applied at points: (a)  $(i = N - 1, j)$ , (b)  $(i = N, j)$ , (c)  $(i' = 0, j)$  and (d)  $(i' = 1, j)$ .

221 the variable  $u$  at point  $\mathbf{x}$  writes [9]:

$$u_{\text{RBF}}(\mathbf{x}) = \sum_{j=1}^{n_v} \xi_j \Phi(\mathbf{x}, \mathbf{x}_j) + \sum_{q=1}^m \zeta_q P_q(\mathbf{x}) \quad (18)$$

222 where  $\xi_j$  and  $\zeta_q$  are the unknown interpolation coefficients,  $(\mathbf{x}_j)_{j=1, \dots, n_v}$  are the  
 223 centers of the  $n_v$  cells,  $\Phi$  are Wendland's radial basis functions [9, 28], and  
 224  $\sum \zeta_q P_q(\mathbf{x}) = \zeta_0 + \zeta_1 x + \zeta_2 y + \dots + \zeta_m z^{\text{deg}(P)}$  is a polynomial term of degree  $\text{deg}(P)$  that  
 225 ensures the unicity of the approximation  $u_{\text{RBF}}$  [18, 29]. The calculation of the coefficients  $\xi_j$  and  
 226  $\zeta_q$  is presented in appendix A.1. Similarly, the value of  $\mathbf{U}$  in the second ghost cell in Fig. 5(a) is  
 227 interpolated using the RBF approximation (18) and  $n_v$  points located at  $i' = 1$ . The choice of the  
 228 interpolation parameters  $n_v$  and  $\text{deg}(P)$  in Eq. (18) is discussed in sections 6 and 7.

229 A second interpolation technique is proposed in order to interpolate the flow variables  $\tilde{\mathbf{U}}$  at the  
 230 block interface  $I'_L$  in Fig. 5(d). As for the interpolation of the flow field in the ghost cells, a RBF  
 231 interpolation is carried out. However, the quantity to interpolate is not a single-point value  $u$  but  
 232 an averaged value  $\tilde{u}$  on a grid interface. Therefore, the interpolation of  $\tilde{u}$  on the interface  $I'_L$   
 233 is performed from  $n_v$  values of  $\tilde{\mathbf{U}}$  at the interfaces  $(I_{R,1}, \dots, I_{R,j'}, I_{R,j'+1}, \dots, I_{R,n_v})$  represented in  
 234 grey in Fig. 5(c). The interpolation formulation at the grid interface  $I'_L$  is obtained by integrating  
 235 Eq (18) on  $I'_L$ :

$$\begin{aligned} \tilde{u}_{L'} &= \frac{1}{|I'_L|} \int_{I'_L} u_{\text{RBF}}(\mathbf{x}) \, d\mathbf{x} \\ &= \sum_{j'=1}^{n_v} \tilde{\xi}_{j'} \left( \frac{1}{|I'_L|} \int_{I'_L} \Phi(\mathbf{x}, \mathbf{x}_{j'}) \, d\mathbf{x} \right) + \sum_{q=1}^m \tilde{\zeta}_q \left( \frac{1}{|I'_L|} \int_{I'_L} P_q(\mathbf{x}) \, d\mathbf{x} \right) \end{aligned} \quad (19)$$

236 where the point  $\mathbf{x}_{j'}$  is the center of the surface  $I_{R,j'}$ . The calculation of the interpolation coefficients  
 237  $\tilde{\xi}_{j'}$  and  $\tilde{\zeta}_q$  is detailed in appendix A.2.1. A 3rd-order Gaussian quadrature is used in order to  
 238 compute the integrals of Eq. (19). In practice, the interpolation coefficients in Eq. (18) and (19)  
 239 are computed only once at the beginning of the simulation and stored in memory, yielding low CPU  
 240 cost interpolations (see appendix A).

241 3.2. Curved interfaces

242 For curved grid interfaces, the flux reconstruction presented in section 3.1 cannot be applied. For the  
 243 interpolation of the flow variables at the grid interface using Eq. (19), as the curvature of the surface  
 244 is not taken into account to define the ghost interface  $I'_L$ , the integral (19) is evaluated on a plane  
 245 interface that does match the shape of the non-conforming interface. Therefore, a flux reconstruction  
 246 for curved non-conforming interfaces is also proposed. The objective is to find a function  $\sigma(\mathbf{x})$  to  
 247 define a curved interface  $I'_{L_{\text{curved}}}$  knowing only the position  $\mathbf{x}$  of the mesh points. The flow variables  
 248 at the interface  $I'_{L_{\text{curved}}}$  are then calculated as in Eq. (19):

$$\begin{aligned} \tilde{u}_{L'} &= \frac{1}{|I'_{L_{\text{curved}}}|} \int_{I'_{L_{\text{curved}}}} u_{\text{RBF}}(\mathbf{x}) \, d\mathbf{x} \\ &= \sum_{j'=1}^{n_v} \tilde{\xi}_{j'} \left( \frac{1}{|I'_{L_{\text{curved}}}|} \int_{I'_{L_{\text{curved}}}} \Phi(\mathbf{x}, \mathbf{x}_{j'}) \, d\mathbf{x} \right) + \sum_{q=1}^m \tilde{\zeta}_q \left( \frac{1}{|I'_{L_{\text{curved}}}|} \int_{I'_{L_{\text{curved}}}} P_q(\mathbf{x}) \, d\mathbf{x} \right) \end{aligned} \quad (20)$$

249 The calculation of the RBF coefficients  $\tilde{\xi}_{j'}$  and  $\tilde{\zeta}_q$  is described in appendix A.2.2.

250 The method to determine the function  $\sigma$  is presented for the 2-D grid of Fig. 7(a), composed  
 251 of two blocks L and R separated by a curved interface. The curved interfaces to be defined by  
 252 the function  $\sigma$  are denoted by  $I'_{L_{\text{curved}}}$  and  $(I_{R,1_{\text{curved}}}, \dots, I_{R,j'_{\text{curved}}}, I_{R,j'+1_{\text{curved}}}, \dots, I_{R,n_v_{\text{curved}}})$ . In  
 253 order to determine the function  $\sigma$ , a technique proposed by Carr et al. [30] for 3-D imaging  
 254 reconstruction is employed. First, relations to be verified by the function  $\sigma$  at given mesh points  
 255 are imposed. In particular, at the  $N_p$  grid points of blocks L and R lying on the interfaces  
 256  $(I_{R,1_{\text{curved}}}, \dots, I_{R,j'_{\text{curved}}}, I_{R,j'+1_{\text{curved}}}, \dots, I_{R,n_v_{\text{curved}}})$  in Fig. 7(a), the function  $\sigma$  cancels out:

$$\sigma(\mathbf{x}_i) = 0 \quad 1 \leq i \leq N_p \quad (21)$$

257 where  $\mathbf{x}_i = (x_i, y_i, z_i)$  are the spatial coordinates of the  $i$ th-mesh point. In order to ensure that  
 258 function  $\sigma$  differs from the zero-function, off-surface points are considered and non-zero values are  
 259 given to the function  $\sigma$  at these points. In the present study,  $n_v$  points of block L and  $n_v$  points of  
 260 block R are selected, corresponding to the centers of the cells adjacent to the grid interface. They  
 261 are represented by black and grey circles in Fig. 7(b) for  $n_v = 3$ . A value of  $\sigma = -1$  is given to the  
 262  $n_v$  points of block L, and  $\sigma = 1$  is attributed to the  $n_v$  points of block R. Thus, the objective is to  
 263 find the function  $\sigma$  so that the following relations are satisfied:

$$\begin{cases} \sigma(\mathbf{x}_i) = 0 & 1 \leq i \leq N_p \\ \sigma(\mathbf{x}_r) = 1 & 1 \leq r \leq n_v \\ \sigma(\mathbf{x}_l) = -1 & 1 \leq l \leq n_v \end{cases} \quad (22)$$

264 where  $(\mathbf{x}_r)_{1,\dots,n_v}$  and  $(\mathbf{x}_l)_{1,\dots,n_v}$  are the positions of the centers of the  $n_v$  cells of blocks L and R,  
 265 respectively. Then, given the set of points  $S_N = [(\mathbf{x}_i)_{1,\dots,N_p}, (\mathbf{x}_r)_{1,\dots,n_v}, (\mathbf{x}_l)_{1,\dots,n_v}] = [(\mathbf{x}_j)_{1,\dots,N_S}]$   
 266 and the relations (22), the function  $\sigma$  is calculated by RBF interpolation [30]:

$$\sigma(\mathbf{x}) \simeq \sigma_{\text{RBF}}(\mathbf{x}) = \sum_{j=1}^{N_S} \Theta_j \Phi(\mathbf{x}, \mathbf{x}_j) + \sum_{q=1}^m \kappa_q P_q(\mathbf{x}) \quad (23)$$

267 where  $N_S = N_p + 2n_v$ , and  $\Theta_j$  and  $\kappa_q$  are the unknown interpolation coefficients computed  
 268 similarly as for the ghost cells (see appendix A.1).

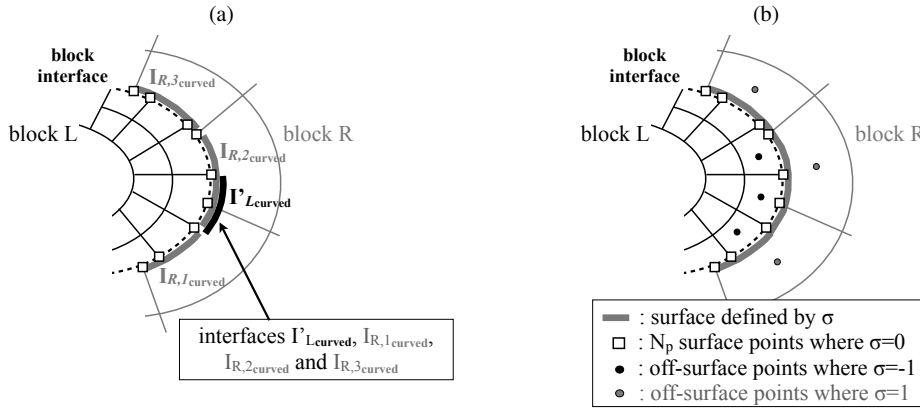


Figure 7. Computation of the function  $\sigma$  that defines the curved interfaces  $I'_{L,curved}$  and  $(I_{R,j,curved})_{1 \leq j \leq n_v=3}$ : (a) interfaces  $I'_{L,curved}$  and  $(I_{R,j,curved})_{1 \leq j \leq 3}$  and  $N_p$  points (squares) lying on the interfaces, (b) surface points (squares) where  $\sigma = 0$  and off-surface points (circles) where  $\sigma \neq 0$ .

#### 4. PROPERTIES OF THE RBF INTERPOLATION IN THE WAVENUMBER SPACE

269 The performance of the RBF interpolation is evaluated in the wavenumber space. For this purpose, a  
 270 uniform 1-D mesh extending over the range  $[0, 1]$ , composed of 81 points  $(x_j)_{1 \leq j \leq 81}$  is considered:

$$x_j = (j - 1)\Delta \quad \text{for } 1 \leq j \leq 81 \quad (24)$$

271 with  $\Delta = 1/80$ . At the points  $x_j$ , a harmonic function  $f_k(x) = \exp(ikx)$  is imposed, where  $k$  is the  
 272 wavenumber with  $k\Delta$  varying from 0 to  $\pi$ , and  $i$  is the complex number verifying  $i^2 = -1$ . For RBF  
 273 interpolations, a second 1-D mesh, referred to as the RBF grid, is defined using  $N_{\text{RBF}} = 41$  points  
 274 located at the following positions:

$$x'_j = \left( 0.2\Delta + \frac{j-1}{N_{\text{RBF}}-1} \right) \quad \text{for } 1 \leq j \leq N_{\text{RBF}} \quad (25)$$

275 In this way, the distance between two consecutive RBF grid points is equal to  $2\Delta$  and there is a full  
 276 point-mismatch between the two 1-D meshes. The interpolation of  $f_k$  on the RBF grid is denoted  $g_k$   
 277 in the following. For consistency with the finite-volume flux reconstruction proposed in this study,  
 278 the function  $g_k$  is defined over each segment  $[x'_j, x'_{j+1}]$ , with  $j \in [1, N_{\text{RBF}} - 1]$ . For  $x \in [x'_j, x'_{j+1}]$ ,

279 from Eq. (18), the function  $g_k$  writes as follows:

$$g_k(x) = \sum_{l=1}^{n_v} \xi_l \Phi(x, x_l) + P(x) \quad (26)$$

280 The  $n_v$  nearest mesh points ( $x_l$ ) that surround point  $x'_{jM} = (x'_j + x'_{j+1})/2$  and where the values  
 281 of  $f_k$  are known are used to determine the interpolation coefficients in Eq. (26). In this section,  
 282 the influence of the number of points  $n_v$  is evaluated by performing interpolations using  $n_v = 4,$   
 283 6, 8 and 20 points. The interpolations are carried out using the 2nd-degree polynomial function  
 284  $P(x) = \zeta_0 + \zeta_1 x + \zeta_2 x^2$ , where  $(\zeta_j)_{0 \leq j \leq 2}$  are the unknown interpolation coefficients. The influence  
 285 of the degree of  $P$  on the accuracy of the spatial discretization is discussed in section 5.

286 First, the accuracy of the RBF interpolation is examined. For this purpose, an interpolation error  $\epsilon$   
 287 is computed as a function of the wavenumber  $k$  from the difference between the values of  $f_k$  and  $g_k$   
 288 over each segment  $[x'_j, x'_{j+1}]$  as:

$$\epsilon(k) = \sum_{j=1}^{N_{\text{RBF}}-1} \int_{x'_j}^{x'_{j+1}} |f_k(x) - g_k(x)| dx \quad (27)$$

289 where  $|\cdot|$  is the complex modulus. Secondly, the energy of the interpolated signal  $g_k$  is compared  
 290 with the energy of the original signal  $f_k$  through the evaluation of the integrals  $E_f$  and  $E_g$  defined  
 291 as:

$$E_f(k) = \int_{x'_1}^{x'_{N_{\text{RBF}}}} |f_k(x)|^2 dx = 1 \quad \text{and} \quad E_g(k) = \int_{x'_1}^{x'_{N_{\text{RBF}}}} |g_k(x)|^2 dx \quad (28)$$

292 For comparison, interpolations are also performed using the polynomial functions of degrees 2 and  
 293 3 given by:

$$P_2(x) = c_1 + c_2 x + c_3 x^2 \quad (29)$$

$$P_3(x) = c_4 + c_5 x + c_6 x^2 + c_7 x^3 \quad (30)$$

294 where  $(c_j)_{1 \leq j \leq 7}$  are the interpolation coefficients. Note that, as for the RBF interpolations, the  
 295 polynomial approximations (29) and (30) are defined by pieces over each segment  $[x'_j, x'_{j+1}]$ .  
 296 The interpolations coefficients  $(c_i)$  are determined using a least-square approximation involving  
 297  $n_v$  nearest points surrounding point  $x'_{jM}$ . More precisely, over each segment  $[x'_j, x'_{j+1}]$ , the values  
 298 of  $(c_i)$  are calculated to minimize the functions  $\chi_{P_2}$  and  $\chi_{P_3}$ :

$$\chi_{P_2}(c_1, c_2, c_3) = \sum_{l=1}^{n_v=4} \frac{|P_2(x_l) - f_k(x_l)|^2}{(x_l - x'_{jM})^2} \quad (31)$$

$$\chi_{P_3}(c_4, c_5, c_6, c_7) = \sum_{l=1}^{n_v=6} \frac{|P_3(x_l) - f_k(x_l)|^2}{(x_l - x'_{jM})^2} \quad (32)$$

299

300 The variations of the energy  $E_g$  obtained from the RBF interpolations using  $n_v = 4, 6, 8$  and  
 301 20 points and from the polynomial interpolations with  $P_2$  and  $P_3$  are represented in Fig. 8(a) as a  
 302 function of the normalized wavenumber  $k\Delta$ . When RBF is used, the value of  $E_g$  decreases with  $k\Delta$ ,

303 indicating higher levels of dissipation at high wavenumbers. The highest levels of dissipation are  
 304 obtained using  $n_v = 4$ . In particular, for  $k\Delta = \pi/3$ , the energy is equal to 0.995 for  $n_v = 4$  whereas  
 305 values  $0.99 < E_g < 1$  are obtained for  $n_v = 6, 8$  and 20. The dissipation obtained using RBF is  
 306 lower than that calculated from a polynomial interpolation of degree 2 over all the wavenumber  
 307 range. In addition, using RBF, no energy amplification is observed whereas energy values  $E_g > 1$   
 308 are found using polynomial interpolation  $P_3$  for  $\pi/8 \leq k\Delta \leq \pi/2$  in Fig. 8(a). Therefore, it is  
 309 interesting to use RBF to preserve the energy stability and to maintain low dissipation levels for  
 310 wavenumbers  $k\Delta < \pi/4$ , which are well resolved by the present spatial discretization schemes.

311 The interpolation errors  $\epsilon$  obtained using RBF and polynomial interpolations are represented in  
 312 Fig. 8(b) as a function of the wavenumber  $k\Delta$ . When RBF is used, the highest values of  $\epsilon$  are  
 313 obtained for  $n_v = 4$ . In this case, the interpolation error is stronger than that calculated with the  
 314 polynomial interpolation  $P_3$  for  $k\Delta < \pi/2$ . However, it is lower than the error computed with  $P_2$   
 315 which involves the same number of interpolation points. When the number of interpolation points  
 316  $n_v$  increases, as expected, the value of  $\epsilon$  decreases all over the wavenumber range. For  $n_v = 20$ , as  
 317 a result, the error  $\epsilon$  is lower than the error computed using  $P_3$  for  $\pi/12 < k\Delta < \pi$ . For  $k\Delta < \pi/12$ ,  
 318 it is higher than that obtained using  $P_3$ , but is very small and lower than  $5 \times 10^{-6}$ .

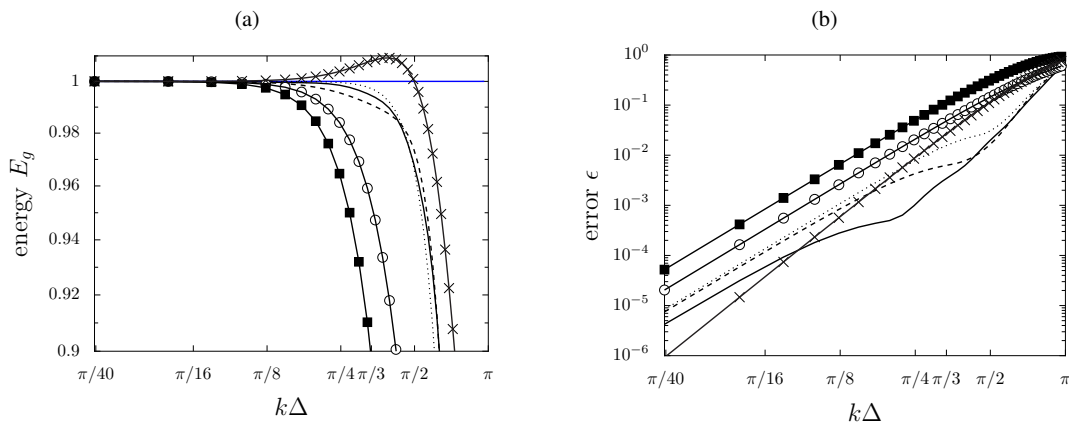


Figure 8. Representation of (a) the energy  $E_g$  and (b) the interpolation error  $\epsilon$  as a function of the normalized wavenumber  $k\Delta$ : RBF interpolations using  $\circ$   $n_v = 4$ ,  $\dots$   $n_v = 6$ ,  $---$   $n_v = 8$ ,  $—$   $n_v = 20$ , polynomial interpolations of  $\blacksquare$  degree 2 and  $\times$  degree 3.  $—$   $E_g = E_f = 1$ .

## 5. ACOUSTIC PULSE

319 In order to examine the overall accuracy of the flux reconstruction presented for non-conforming  
 320 grids above, an acoustic pulse is imposed in the vicinity of a non-conforming interface in a medium  
 321 at rest. For this purpose, the two-dimensional domain of size  $\ell \times \ell$  shown in Fig. 9(a) is considered,  
 322 with  $\ell = 100$  m. It is composed of two blocks separated by a non-conforming interface located at

323  $x = 0.6\ell$ . At  $t = 0$ , the pulse is introduced at  $x_p = 0.4\ell$  and  $y_p = 0.5\ell$  as:

$$\begin{cases} \rho'(x, y) = A_p \exp\left(-\ln 2 \frac{(x - x_p)^2 + (y - y_p)^2}{\bar{h}^2}\right) \\ u'(x, y) = v'(x, y) = 0 \\ p'(x, y) = c_0^2 \rho'(x, y) \end{cases} \quad (33)$$

324 where  $\bar{h} = 0.03\ell$  is the pulse half-width,  $A_p$  is the pulse amplitude, and  $c_0$  is the ambient sound  
325 speed. The ambient pressure and temperature are equal to  $p_0 = 10^5$  Pa and  $T_0 = 300$  K, respectively.  
326 Radiation boundary conditions and sponge layers are used. An exact solution of the problem can be  
327 derived from the linearized Euler equations [31]. In order to compare the numerical results obtained  
328 from the Navier-Stokes equations with the exact solution, an amplitude  $A_p$  of 0.1 Pa is chosen. In  
329 addition, the viscous terms in Eq. (1) are neglected in the simulations.

330 The performance of the flux reconstruction is evaluated using six Cartesian grids referred  
331 to as pulsegrid1, pulsegrid2, pulsegrid3, pulsegrid4, pulsegrid5 and pulsegrid6, and two flux  
332 reconstruction techniques with and without RBF interpolation. The RBF interpolations are carried  
333 out using a number of  $n_v = 8$  points. The influence of the degree  $\text{deg}(P)$  of the RBF polynomial  
334 function in Eq. (18) is examined using polynomial functions of degree 0, 1 and 2. For the flux  
335 reconstruction without RBF, 2nd-order interpolations are used in order to reconstruct the flow  
336 variables in the ghost cells and at the grid interface [32]. This reconstruction, available in the *elsA*  
337 solver [20], is described in appendix A.3.

338 The mesh parameters, namely the grid spacings  $\Delta x$ , and the grid spacings  $\Delta y^L$  and  $\Delta y^R$  at the  
339 left and right hand sides of the block interface are given in Tab. I. The meshes pulsegrid2, pulsegrid3,  
340 pulsegrid4, pulsegrid5 and pulsegrid6 are respectively 2, 3, 4, 5 and 6 times finer than pulsegrid1.  
341 In all cases, at the left-hand side of the interface, a uniform grid spacing  $\Delta x = \Delta y^L$  is used in the  
342 directions  $x$  and  $y$ . For pulsegrid1, it is equal to  $0.02\ell$ . At the right hand-side of the interface, the  
343 grid spacing is also equal to  $\Delta x$  in  $x$  direction whereas the mesh spacing  $\Delta y^R$  is twice larger than  
344  $\Delta y^L$  in  $y$  direction. In order to have a full point-mismatch at the grid interface, for  $x > 0.6\ell$ , in all  
345 cases, the grid cells are shifted upwards of  $0.5\Delta y^L$ .

mesh	$\Delta x$	$\Delta y^L$	$\Delta y^R$
pulsegrid1	$\ell/50$	$\ell/50$	$\ell/25$
pulsegrid2	$\ell/100$	$\ell/100$	$\ell/50$
pulsegrid3	$\ell/150$	$\ell/150$	$\ell/75$
pulsegrid4	$\ell/200$	$\ell/200$	$\ell/100$
pulsegrid5	$\ell/250$	$\ell/250$	$\ell/125$
pulsegrid6	$\ell/300$	$\ell/300$	$\ell/150$

Table I. Mesh spacings used in the simulations of the pulse.

346 The time step  $\Delta t$  of the simulations is chosen sufficiently small so that the errors related to  
347 the time discretization are negligible. More precisely, its value is calculated in order to provide  
348 a CFL number  $c_0\Delta t/\Delta x$  of 0.05 for  $\Delta x = \ell/300$ . The fluctuating pressure field  $p'$  obtained at  
349  $t = 1200\Delta t$  using pulsegrid2 is represented in Fig. 9(a). At this instant, the acoustic wave reaches  
350 the non-conforming interface. In order to evaluate the effective order of the spatial discretization  
351 in the presence of the non-conforming interface, the pressure fluctuation obtained at  $t = 1200\Delta t$  is



352 compared to the exact solution  $p'_{\text{exact}}$  through the  $L_2$  relative error:

$$\epsilon_p = \left( \frac{\int_{\Omega_\epsilon} (p' - p'_{\text{exact}})^2 d\Omega}{\int_{\Omega_\epsilon} p_{\text{exact}}^2 d\Omega} \right)^{1/2} \quad (34)$$

353 where  $\Omega_\epsilon = \{(x, y) \in \mathbb{R}^2 \mid 0.2\ell \leq x, y \leq 0.8\ell\}$ . In finite-volume,  $p'$  is the averaged value of the  
 354 fluctuating pressure over each cell of domain  $\Omega_\epsilon$  (see Eq. (8)). Therefore, for consistency, the exact  
 355 solution is calculated similarly. The discrete form of Eq. (34) thus writes as:

$$\epsilon_p = \left( \frac{\sum_{\text{cell} \in \Omega_\epsilon} (p' - p'_{\text{exact cell}})^2}{\sum_{\text{cell} \in \Omega_\epsilon} p_{\text{exact cell}}^2} \right)^{1/2} \quad (35)$$

356 where  $p'_{\text{exact cell}} = (1/|\Omega_{\text{cell}}|) \int_{\Omega_{\text{cell}}} p'_{\text{exact}} d\Omega$  and  $|\Omega_{\text{cell}}|$  is the volume of the cell. Simulations with  
 357 four uniform Cartesian meshes without grid interfaces with grid spacings of  $\Delta x = \Delta y = \ell/50$ ,  
 358  $\ell/100$ ,  $\ell/200$  and  $\ell/300$  respectively have also been done for comparisons.

359 The errors  $\epsilon_p$  obtained using the non-conforming grids with and without the flux reconstruction  
 360 based on RBF for polynomial functions of degrees 0, 1 and 2 are presented in Fig 9(b), as a function  
 361 of the grid spacing  $\Delta x/\ell$ . Those obtained using the meshes without grid interface are also indicated.  
 362 In all cases, the amplitude of  $\epsilon_p$  decreases as the value of  $\Delta x$  tends to 0. Using the grid without  
 363 interface, the error profile follows a 6th-order convergence slope. This result is expected since the  
 364 present spatial discretization is based on 6th-order numerical schemes (see Fosso *et al.* [12]). With  
 365 non-conforming interfaces, the 6th-order convergence slope is not retrieved, and higher error levels  
 366 are obtained for  $\Delta x \leq 0.005\ell$  compared to the simulations without interfaces. The stronger errors  
 367 are obtained using the flux reconstruction without RBF, with an error profile varying following a  
 368 2nd-order slope. When RBF is used, lower errors are obtained, and they decrease with the degree  
 369 of  $P$ . In particular, the error profile calculated with  $\text{deg}(P)=2$  is in good agreement with that  
 370 obtained for conforming grids. In the following, the RBF interpolations are therefore performed  
 371 using  $\text{deg}(P)=2$ .

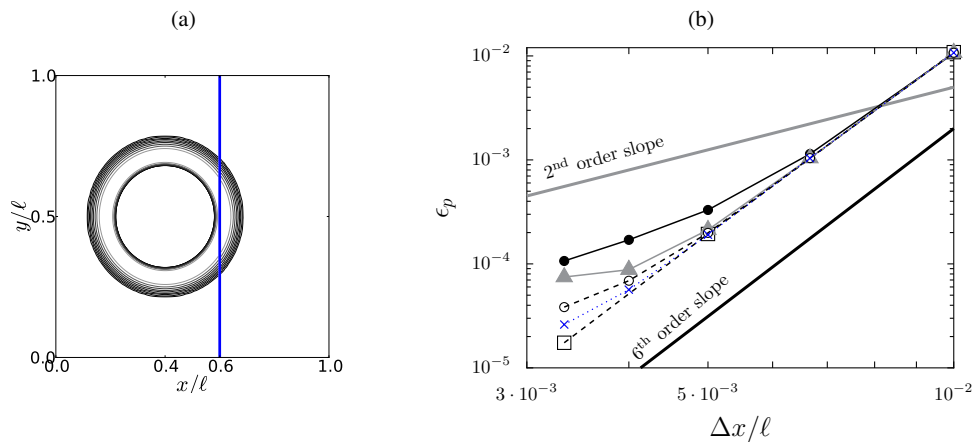


Figure 9. (a) Fluctuating pressure  $p'$  at  $t = 1200\Delta t$  using pulsegrid2, with 10 isocontours from  $10^{-4}$  to  $10^{-2}$  Pa following a geometric progression of ratio 1.67. The non-conforming interface is shown in blue. (b) Error profiles  $\epsilon_p$  as a function of the grid spacing  $\Delta x/\ell$ : RBF interpolations with polynomial functions  $\blacktriangle$   $\text{deg}(P)=0$ ,  $\circ$   $\text{deg}(P)=1$ ,  $\times$   $\text{deg}(P)=2$ ,  $\bullet$  interpolation without RBF and  $\square$  grids without interface.

## 6. CONVECTION OF A VORTEX

372 The performance of the flux reconstruction on non-conforming grids is then evaluated by performing  
373 2-D simulations of vortex convection on Cartesian and wavy meshes.

374 *6.1. Cartesian grids*

375 A round vortex is convected in a mean flow defined by a uniform Mach number  $M$  of 0.5, a pressure  
376 of  $10^5$  Pa and a temperature of 300 K. The two-dimensional computational domain used in the  
377 simulations extends from  $x = 0$  down to  $x = 3L$  in the streamwise direction, and from  $y = 0$  up  
378 to  $y = L$  in the transverse direction, where  $L = 0.1$  m. It is divided into two blocks separated by  
379 a vertical non-conforming interface located at  $x = L$ . The vortex is defined by the velocity and  
380 pressure fluctuations:

$$\begin{cases} u' = -\frac{\Gamma}{R^2}(y - y_c) \exp\left(-\ln 2 \frac{(x - x_c)^2 + (y - y_c)^2}{2b^2}\right) \\ v' = \frac{\Gamma}{R^2}(x - x_c) \exp\left(-\ln 2 \frac{(x - x_c)^2 + (y - y_c)^2}{2b^2}\right) \\ p' = -\frac{\rho\Gamma^2}{2R^2} \exp\left(-\ln 2 \frac{(x - x_c)^2 + (y - y_c)^2}{b^2}\right) \end{cases} \quad (36)$$

381 where  $(x_c = 0.5L, y_c = 0.5L)$  is the position of the vortex center at the initial time  $t = 0$ ,  
382  $b = (\sqrt{\ln 2}/20)L \simeq 0.04L$  is the vortex Gaussian half-width, and  $\Gamma$  represents the vortex intensity  
383 given by:

$$\frac{\rho\Gamma^2}{2R^2} = 10^3 \text{ Pa} \quad (37)$$

384 where  $R = b/\sqrt{\ln 2}$ . The velocity and pressure fluctuations are superimposed onto the mean flow at  
385  $t = 0$ .

386 The performance of the flux reconstruction is examined by performing simulations using  
387 four meshes referred to as Finegrid, Mediumgrid, Coarsegrid, and Verycoarsegrid, and two flux  
388 reconstruction techniques with and without RBF interpolations. When RBF is applied, the influence  
389 of the number of interpolation points  $n_v$  is studied by carrying out interpolations with  $n_v = 4$ ,  
390 6, 8 and 12 points. The RBF interpolations are performed using a second-degree polynomial  
391 function in Eq. (18). The influence of the degree of the polynomial function has been examined  
392 by performing simulations using polynomial functions of degrees 0, 1 and 2. The use of the second-  
393 degree polynomial function provided the lowest spurious noise levels at the grid interface. For the  
394 sake of concision, these results are not presented in this study. Views of the four meshes close to  
395 the block interface are given in Fig. 10. The mesh parameters, including the grid spacings  $\Delta x$  in  
396 the streamwise direction, and the grid spacings  $\Delta y^L$  and  $\Delta y^R$  at the left and the right sides of  
397 the block interface are provided in Tab. II. In all cases, in the streamwise direction, a grid spacing  
398 of  $\Delta x = \Delta = L/255$  is used. The vortex half-width  $b$  is thus discretized by 10 points, given that  
399  $b = 10.6\Delta$ . In the transverse direction, on the left hand side of the interface, the grid spacing  $\Delta y^L$   
400 is equal to  $\Delta$ . On the right hand side, the mesh resolution in the  $y$  direction is different from  $\Delta$ .  
401 More precisely, the grid spacing  $\Delta y^R$  is respectively equal to  $0.5\Delta$ ,  $2\Delta$ ,  $4\Delta$  and  $6\Delta$  for Finegrid,  
402 Mediumgrid, Coarsegrid and Verycoarsegrid, corresponding to a discretization of the vortex half-  
403 width by 21.2, 5.3, 2.6 and 1.8 points. In addition, in order to ensure a full point-mismatch at the

404 grid interface, for  $x > L$ , the cells are shifted upwards of  $\Delta y^R/2$  for Finegrid and of  $\Delta y^L/2$  for the  
 405 meshes Mediumgrid, Coarsegrid and Verycoarsegrid.

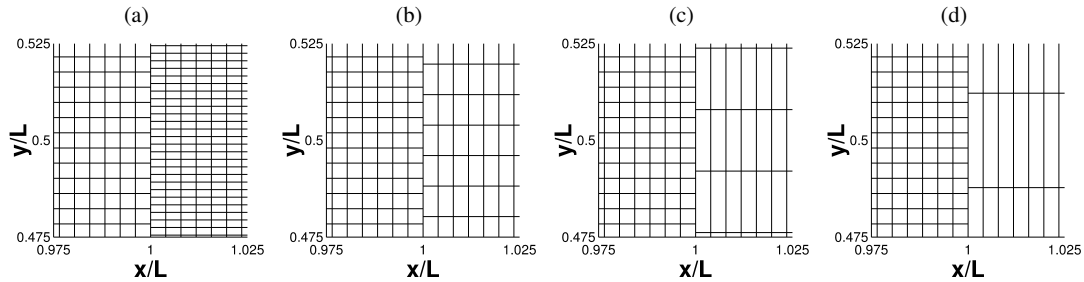


Figure 10. Representation of the meshes close to the block interface: (a) Finegrid, (b) Mediumgrid, (c) Coarsegrid, and (d) Verycoarsegrid.

mesh	$\Delta x$	$\Delta y^L$	$\Delta y^R$
Finegrid	$\Delta$	$\Delta$	$0.5 \Delta$
Mediumgrid	$\Delta$	$\Delta$	$2 \Delta$
Coarsegrid	$\Delta$	$\Delta$	$4 \Delta$
Verycoarsegrid	$\Delta$	$\Delta$	$6 \Delta$

Table II. Mesh spacings for the Fine, Medium, Coarse, and Verycoarse grids.

406 The time step  $\Delta t$  in the computations is chosen in order to impose a CFL number  
 407  $(1 + M)c_0\Delta t/\Delta$  of 0.4, where  $c_0$  is the ambient sound speed. When the vortex crosses the block  
 408 interface, spurious waves are generated due to the difference in grid resolution as well as to the  
 409 specific spatial discretization at the interface. The objective here is to ensure that the amplitude  
 410 of these spurious waves is very low with respect to the pressure deficit in the vortex. For that,  
 411 the pressure field  $p_{\text{interface}}$  obtained in the multiblock simulations is compared with the pressure  
 412 field  $p_{\text{no-interface}}$  computed from a simulation without block interface. That monoblock simulation is  
 413 carried out using the same computational domain with mesh spacings  $\Delta x = \Delta y = \Delta$ . By comparing  
 414 the pressure  $p_{\text{interface}}$  with  $p_{\text{no-interface}}$  instead of with the analytical vortex solution (36), the error  
 415 thus obtained only results from the effects of the non-conforming grid and not from discretization  
 416 errors. In addition, the pressure field differences  $\Delta p = p_{\text{interface}} - p_{\text{no-interface}}$  are only computed at  
 417 the left side of the block interface where the mesh is similar in the two computations. In this way,  
 418 the pressure fields  $p_{\text{interface}}$  and  $p_{\text{no-interface}}$  are computed at the same point. In particular, the time  
 419 evolution of  $\Delta p$  is recorded at the two mesh points A and B, indicated by squares in Fig. 11. They  
 420 are located, respectively, at the interface at  $x = L$  and  $y = 0.5L$ , and upstream of the block interface  
 421 at  $x = 0.8L$  and  $y = 0.75L$ . The signal recorded at point A provides information on the vortex  
 422 deformation at the block interface, while the signal at point B gives the amplitude of the spurious  
 423 waves propagating from the interface.

424 **6.1.1. Grid sensitivity** The influence of the mesh resolution is evaluated by performing four  
 425 simulations using Finegrid, Mediumgrid, Coarsegrid and Verycoarsegrid. The simulation settings  
 426 are given in Tab. III. In the four simulations, the flux reconstruction at the block interface is

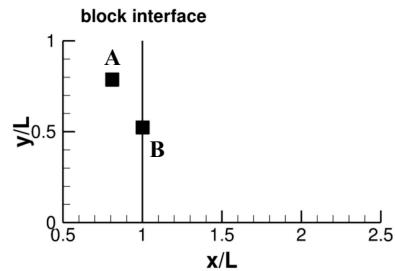


Figure 11. Representation of the mesh points A and B (squares) where the pressure field is recorded.

427 performed using RBF, with interpolations on  $n_v = 8$  points and the second-degree polynomial  
function  $(P_q)_{(1,\dots,m)} = (1, x, y, x^2, y^2, xy)$ .

mesh	flux reconstruction technique	$n_v$	RBF polynomial degree
<b>Finegrid</b>	RBF	8	2
<b>Mediumgrid</b>	RBF	8	2
<b>Coarsegrid</b>	RBF	8	2
<b>Verycoarsegrid</b>	RBF	8	2

Table III. Parameters of the simulations in the grid sensitivity study.

428

429 The time evolution of the pressure  $|\Delta p| = |p_{\text{interface}} - p_{\text{no-interface}}|$  recorded at points A and B in  
430 the simulations is presented in Fig. 12, where  $|\cdot|$  is the absolute value. The vertical blue line in the  
431 figures indicates the moment when the vortex hits the block interface. The signal amplitudes are  
432 displayed in log scale in order to enhance the differences between the simulations. At point A, in  
433 Fig. 12(a), the maximum value of  $|\Delta p|$  is obtained at the instant when the vortex crosses the interface  
434 in all cases. Using Verycoarsegrid, the pressure fluctuation peak is equal to 28.1 Pa, corresponding  
435 to 2.7% of the pressure at the center of the vortex. Using Coarsegrid, the pressure difference reaches  
436 a value of 5 Pa. Using the medium and the refined meshes, the amplitudes of the spurious waves at  
437 point A are significantly lower than those found for the coarse grids, and do not exceed 0.9 Pa and  
438 0.2 Pa, respectively. At point B in Fig 12(b), the noise level also decreases as the mesh is refined at  
439 the right hand side of the block interface. Indeed, maximum pressure differences of 3.6 Pa, 0.4 Pa,  
440 0.1 Pa and 0.03 Pa are obtained in Verycoarsegrid, Coarsegrid, Mediumgrid and Finegrid. These  
441 levels are much lower than those at point A. Note that using Verycoarsegrid, the vortex half-width  $b$   
442 is only discretized by 1.8 points at the right side of the block interface. As a consequence, the mesh  
443 is not fine enough and the vortex structure is strongly modified when it crosses the block interface,  
444 yielding  $|\Delta p| > 0.5$  Pa at points A and B for  $t > 10000\Delta t$ . These results demonstrate that non-  
445 conforming grids must be designed such that the flow field is correctly discretized at both sides  
446 of the interface. In the present simulations, given the vortex Gaussian half-width  $b$ , a grid spacing  
447  $\Delta y^R \leq 4\Delta$  is recommended, corresponding to a discretization of the half-width  $b$  by 2.6 points  
448 (i.e 5.2 points in the vortex width). This result was expected since the numerical methods used  
449 in this study well-calculate the scales discretized by at least 5 points per wavelength [14]. Let us  
450 mention that values  $\Delta y^R > 4\Delta$  could be used in sponge zones, that is to say in flow regions close  
451 to the domain boundaries where the mesh is deliberately coarse in order to damp hydrodynamic  
452 fluctuations before they reach the boundary conditions.

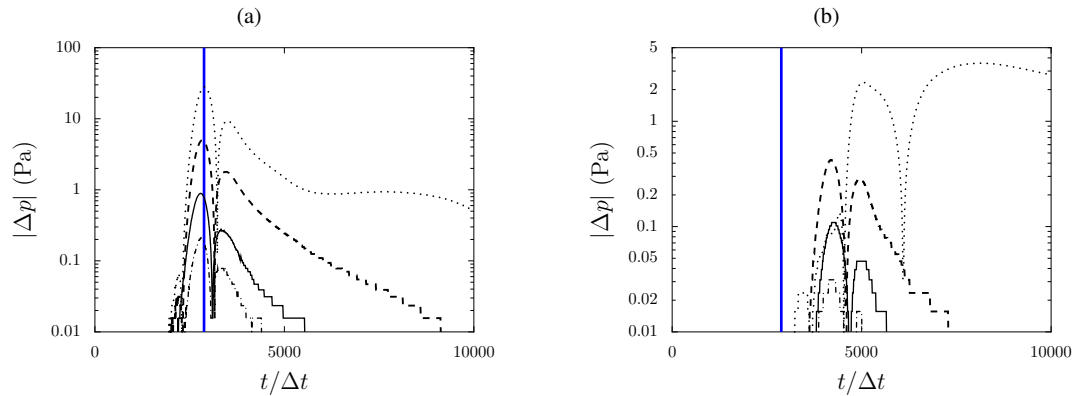


Figure 12. Representation of the time evolution of the pressure difference  $|\Delta p| = |p_{\text{interface}} - p_{\text{no-interface}}|$  (a) at point A and (b) at point B:  $\cdots$  Finegrid,  $\text{—}$  Mediumgrid,  $\text{---}$  Coarsegrid, and  $\text{-}\cdot\cdot\cdot$  Verycoarsegrid. The vertical blue line indicates the moment when the vortex hits the interface.

453 *6.1.2. Influence of the number of points used for RBF interpolations* In order to study the  
 454 influence of the number of points  $n_v$  used for RBF interpolations, four simulations are carried  
 455 out using  $n_v = 4, 6, 8$  and  $12$  points respectively. The simulation parameters are given in Tab. IV.  
 456 The medium grid with mesh spacings  $\Delta x = \Delta y^L = \Delta$  and  $\Delta y^R = 2\Delta$ , and the second-degree  
 polynomial function for RBF interpolation are used in all cases.

mesh	flux reconstruction technique	$n_v$	RBF polynomial degree
Mediumgrid	RBF	<b>4</b>	2
Mediumgrid	RBF	<b>6</b>	2
Mediumgrid	RBF	<b>8</b>	2
Mediumgrid	RBF	<b>12</b>	2

Table IV. Parameters of the simulations in the study of the influence of the number of points for RBF interpolations.

457  
 458 The time variations of the pressure difference  $\Delta p = p_{\text{interface}} - p_{\text{no-interface}}$  recorded at points A and  
 459 B are displayed in Fig. 13. The maximum spurious noise levels are observed using  $n_v = 4$ , when  
 460 interpolations are performed using 4 points. In this case, peaks of 1.6 Pa and 0.3 Pa are obtained  
 461 at the interface and upstream. When interpolations are carried out on 6 points, the noise levels are  
 462 reduced by at least 60% at both points A and B compared to the case using  $n_v = 4$ . Increasing the  
 463 number of interpolation points from 6 to 8 also leads to a decrease of noise levels upstream of the  
 464 block interface in Fig. 13(b), whereas no improvement is found at the interface in Fig. 13(a). Finally,  
 465 the pressure signals obtained using  $n_v = 8$  and  $12$  have similar shapes suggesting that using 8 points  
 466 for RBF interpolations is sufficient to reach accurate results in the present test case.

467 *6.1.3. Influence of the flux reconstruction technique* In this section, the performance of the flux  
 468 reconstruction based on RBF interpolations is compared with that of a flux reconstruction without  
 469 RBF. The flux reconstruction without RBF, available in the *elsA* solver [20], is described in  
 470 appendix A.3. In the following, four simulations are performed with and without RBF, using  
 471 Mediumgrid and Coarsegrid. The simulation parameters are provided in Tab. V. The RBF  
 472 interpolations are carried out using  $n_v = 8$  points and the second-degree polynomial function.

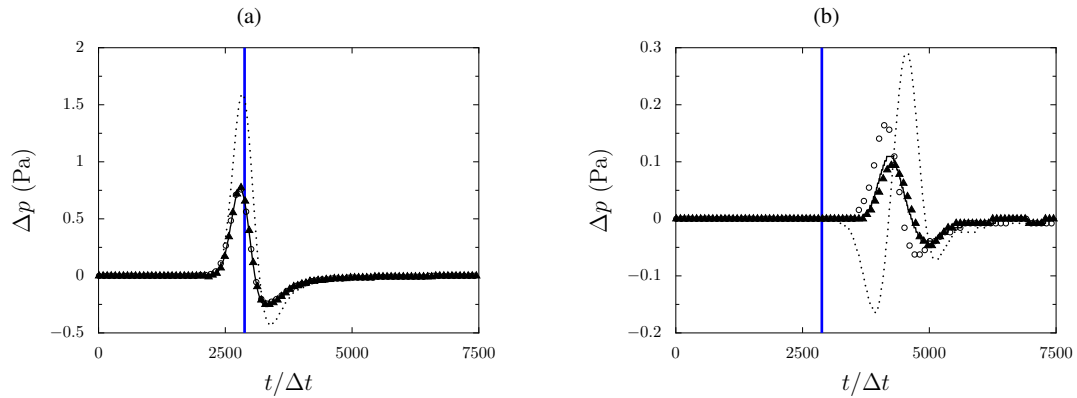


Figure 13. Representation of the time evolution of the pressure difference  $\Delta p = p_{\text{interface}} - p_{\text{no-interface}}$  (a) at point A and (b) at point B:  $\cdots n_v = 4$ ,  $\circ n_v = 6$ ,  $\blacktriangle n_v = 8$  and  $\text{—} n_v = 12$  points. The vertical blue line indicates the moment when the vortex hits the interface.

473 The time variations of the pressure error  $\Delta p$  obtained at points A and B in the simulations using  
 474 Mediumgrid are presented in Fig. 14. The flux reconstruction technique without RBF provides  
 475 higher noise levels compared to the technique using RBF, especially at point B where the signal  
 476 amplitude is 7.5 times higher. The pressure signals obtained using Coarsegrid are displayed in  
 477 Fig. 15. Using the RBF technique, maximum values of 5 Pa and 0.45 Pa are reached at points  
 478 A and B, whereas values of 17.8 Pa and 2 Pa are obtained without RBF. Thus, the use of the flux  
 479 reconstruction technique based on RBF allows us to reduce both the modifications of the vortex  
 480 structure and the generation of spurious pressure waves at the block interface.

mesh	flux reconstruction technique	$n_v$	RBF polynomial degree
<b>Mediumgrid</b>	<b>RBF</b>	8	2
<b>Mediumgrid</b>	<b>no RBF</b>	8	2
<b>Coarsegrid</b>	<b>RBF</b>	8	2
<b>Coarsegrid</b>	<b>no RBF</b>	8	2

Table V. Parameters of the simulations in the study of the influence of the flux reconstruction technique.

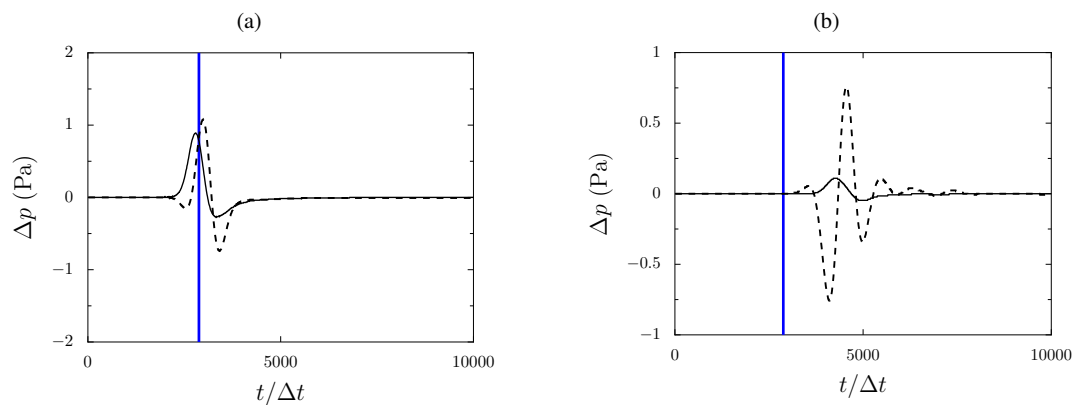


Figure 14. Representation of the time evolution of the pressure difference  $\Delta p = p_{\text{interface}} - p_{\text{no-interface}}$  (a) at point A and (b) at point B using Mediumgrid:  $\text{—}$  RBF,  $\text{---}$  no RBF. The vertical blue line indicates the moment when the vortex hits the interface.

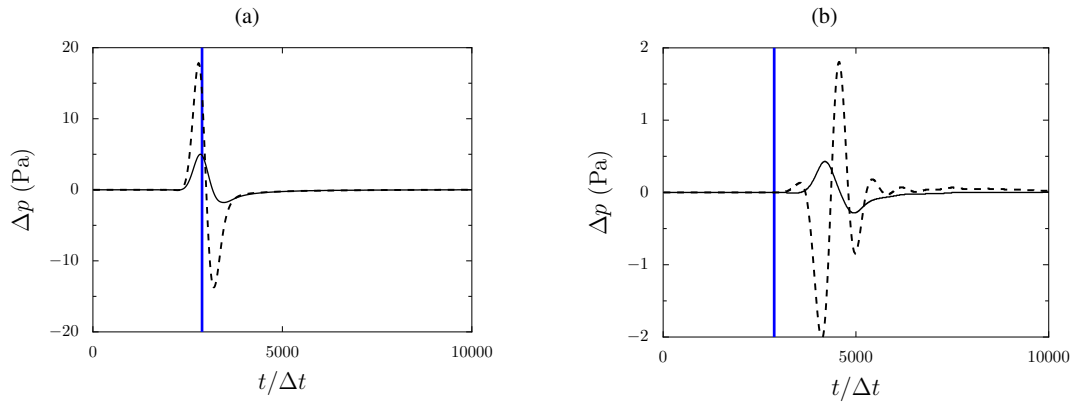


Figure 15. Representation of the time evolution of the pressure difference  $\Delta p = p_{\text{interface}} - p_{\text{no-interface}}$  (a) at point A and (b) at point B using Coarsegrid: — RBF, - - - no RBF. The vertical blue line indicates the moment when the vortex hits the interface.

## 481 6.2. Wavy grids

482 In order to examine the performance of the flux reconstruction for curved non-conforming  
 483 interfaces, the vortex defined in section 6.1 is convected on 2-D wavy grids. Three computational  
 484 domains, presented in Fig. 16, are considered. They are composed of 2 blocks separated by a wavy  
 485 non-conforming interface located close to  $x = L$ , where  $L = 0.1$  m. The wavy grid interfaces are  
 486 defined by a sinusoidal shape of wavelength  $\lambda_x$  and of amplitude  $\lambda_y$ . The values of  $\lambda_x$  and  $\lambda_y$  are  
 487 provided in Tab. VI for the different meshes. In the grid referred to as wavy1, the block interface  
 488 has a height of  $\lambda_y = 24b$  and a sinusoidal shape of amplitude of  $\lambda_x = 8b$ , where  $b$  is the vortex half-  
 489 width. In wavy2, the amplitude of the sinusoidal interface is two times higher than in wavy1, i.e.  
 490  $\lambda_x = 16b$ , but  $\lambda_y = 24b$  as previously. In wavy3, the block interface is composed of three sinusoidal  
 491 arches with  $\lambda_x = \lambda_y = 8b$ . In all cases, a grid spacing  $\Delta x = \Delta = L/127$  is used in the  $x$  direction,  
 492 leading to a vortex half-width discretized by 5.3 points. In the  $y$  direction, the grid spacing is equal  
 493 to  $\Delta y^L = \Delta$  at the left hand side of the interface. In order to create non-conforming grids, a mesh  
 494 spacing  $\Delta y^R = L/87$  is applied at the right hand side of the interface, yielding  $b = 2.6\Delta$ . The  
 495 vortex, convected from the left to the right, is initially located at  $y_0 = 0.5L$ , and at equal distance  
 496 from the domain inlet and the block interface in the  $x$  direction.

mesh	$\lambda_x$	$\lambda_y$
wavy1	$8b$	$24b$
wavy2	$16b$	$24b$
wavy3	$8b$	$8b$

Table VI. Parameters of the wavy grid interfaces.

497 Six simulations are performed using wavy1, wavy2 and wavy3, and the flux reconstructions  
 498 designed for plane and curved interfaces. Their parameters are given in Tab. VII. In all cases,  
 499 RBF interpolations are carried out using a number of  $n_v = 8$  points and the second-degree  
 500 polynomial function. The time step  $\Delta t$  in the computations is chosen such that CFL number  
 501  $(1 + M)c_0\Delta t/\Delta=0.2$ .

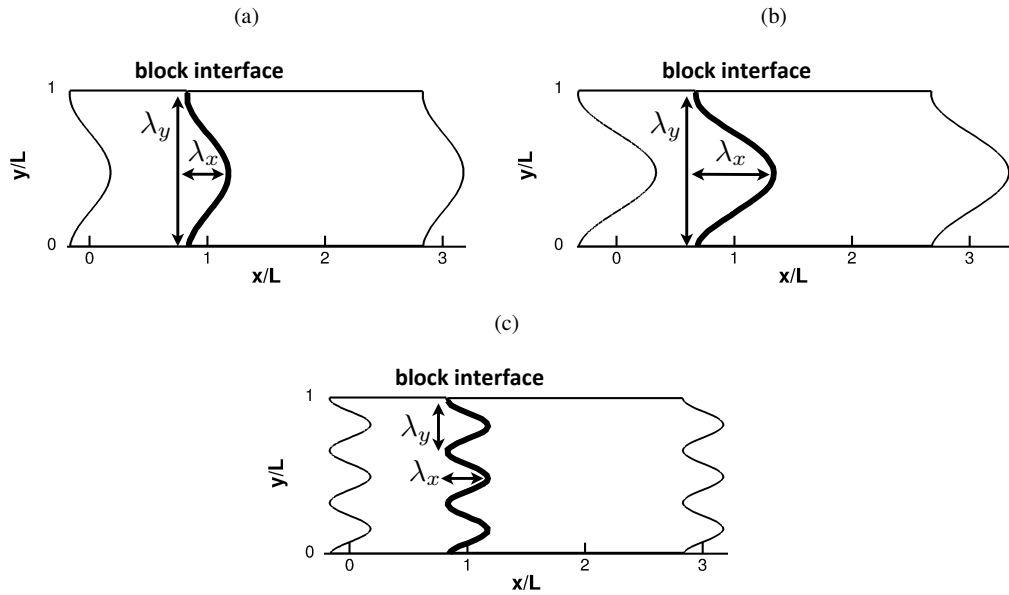


Figure 16. Representation of the wavy computational domains: (a) wavy1, (b) wavy2, and (c) wavy3. The non-conforming interface is indicated by a bold line.

502 The spurious noise generated at the block interface is not recorded at specific points as for the  
 503 Cartesian grids in section 6.1. Indeed, since the shapes of the block interfaces in wavy1, wavy2, and  
 504 wavy3 differ, the distance between a given point and the interface is not identical in the three grids.  
 505 Therefore, the computation of the pressure difference  $\Delta p = p_{\text{interface}} - p_{\text{no-interface}}$  at specific points  
 506 is not relevant. Instead, the pressure difference is determined over all the computational domain.  
 507 In order to compute the pressure field  $p_{\text{no-interface}}$ , for each wavy grid, two simulations are carried  
 508 out using conforming meshes. The first conforming mesh coincides with the non-conforming grid  
 509 at the left-hand side of the interface, whereas the second mesh matches the resolution of the non-  
 510 conforming grid at the right-hand side.

mesh	flux reconstruction technique	$n_v$	RBF polynomial degree
<b>wavy1</b>	<b>RBF curve</b>	8	2
<b>wavy2</b>	<b>RBF curve</b>	8	2
<b>wavy3</b>	<b>RBF curve</b>	8	2
<b>wavy1</b>	<b>RBF plane</b>	8	2
<b>wavy2</b>	<b>RBF plane</b>	8	2
<b>wavy3</b>	<b>RBF plane</b>	8	2

Table VII. Parameters of the simulations in the study of the influence of the flux reconstruction technique for curved interfaces.

511 Snapshots of the pressure difference  $\Delta p$  obtained at  $t = 2800\Delta t$  using wavy1 and the flux  
 512 reconstruction for plane and curved interfaces are presented in Fig. 17. At this time, the vortex  
 513 core is located at  $x = 1.5L$ . In both cases, the presence of the non-conforming grid interface results  
 514 in a significant discretization error around the vortex core as well as in the emission of spurious  
 515 pressure waves of amplitude about 10 Pa. The simulation using the flux reconstruction technique  
 516 designed for curved interfaces provides a maximum noise level of 5.2 Pa, which is two times lower  
 517 than that obtained in the simulation using the reconstruction for plane interfaces.



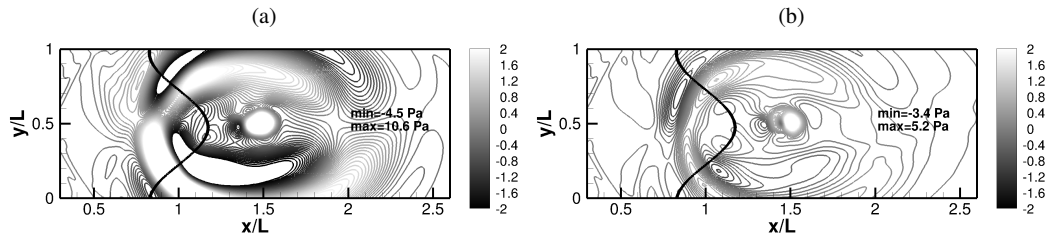


Figure 17. Representation of the pressure difference  $\Delta p$  at  $t = 2800\Delta t$  using way1: flux reconstruction for (a) plane interfaces and (b) curved interfaces, levels given in Pa.

518 The pressure difference  $\Delta p$  obtained at  $t = 2800\Delta t$  using way2 is plotted in Fig. 18. Noise levels  
 519 of 10-20 Pa are found. They are higher compared to the results obtained using way1 in Fig. 17. This  
 520 is due to the block interface which displays stronger variations than that using way1. The pressure  
 521 difference obtained in Fig. 18 (a) with the flux reconstruction technique for curved interfaces shows  
 522 weaker pressure wave amplitudes compared to the pressure difference obtained in Fig. 18 (b) for  
 523 the plane interface reconstruction.

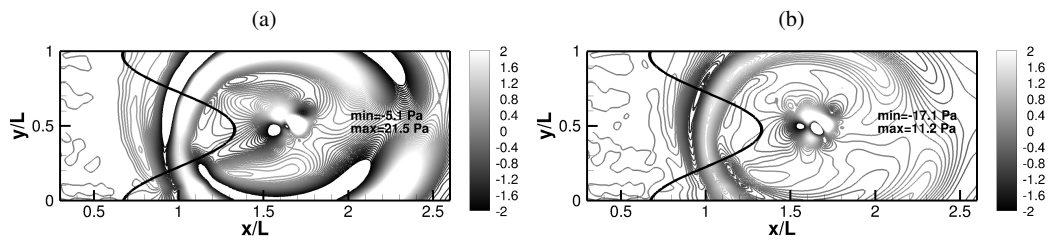


Figure 18. Representation of the pressure difference  $\Delta p$  at  $t = 2800\Delta t$  using way2: flux reconstruction for (a) plane interfaces and (b) curved interfaces, levels given in Pa.

524 Snapshots of the pressure difference  $\Delta p$  obtained using way3 at  $t = 2800\Delta t$  are displayed in  
 525 Fig. 19. As for way1 and way2, lower spurious noise is found using the curved reconstruction  
 526 technique than the plane one. However, the use of a block interface with 3 arches generates higher  
 527 spurious noise levels than previously, with maximum values of  $\Delta p$  of 200 Pa reached at this  
 528 instant. In particular, the vortex core, located at  $x = 1.5L$  is strongly affected by the presence of  
 529 the block interface. The use of non-conforming interfaces with low curvature therefore seems to be  
 530 recommended.

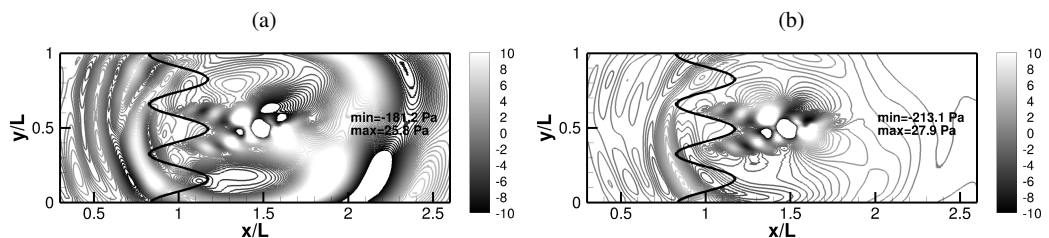


Figure 19. Representation of the pressure difference  $\Delta p$  at  $t = 2800\Delta t$  using way3: flux reconstruction for (a) plane interfaces and (b) curved interfaces, levels given in Pa.

## 7. THREE-DIMENSIONAL JET

531 In order to demonstrate the applicability of the flux reconstruction technique to a 3-D simulation,  
 532 a circular isothermal jet is computed using a Cartesian mesh with a non-conforming interface. The  
 533 aim is to prove that the use of non-conforming interfaces does not significantly affect the jet flow  
 534 development and the sound field radiated by the jet in the near-field region.

## 535 7.1. Jet definition

536 The jet flow has a Mach number of  $M = u_j/c_0 = 0.9$  and a Reynolds number of  
 537  $Re_D = u_j D/\nu = 4 \times 10^5$ , corresponding to the conditions of the jet in the numerical simulation  
 538 of Bogey and Bailly [33], where  $D$  and  $u_j$  are the jet diameter and velocity,  $c_0$  is the sound speed  
 539 and  $\nu$  is the molecular viscosity. The ambient pressure  $p_0$  and temperature  $T_0$  are respectively equal  
 540 to  $10^5$  Pa and 300 K. The jet inflow, located at  $x = 0$ , is characterized by the mean longitudinal  
 541 velocity profile given by the hyperbolic tangent-profile:

$$u(r) = \frac{1}{2}u_j \left( 1 + \tanh \left( \frac{r_0 - r}{2\delta_\theta} \right) \right) \quad (38)$$

542 where  $\delta_\theta = r_0/20$  is the initial momentum thickness of the shear layer,  $r_0 = D/2$  is the jet radius,  
 543 and  $r = \sqrt{y^2 + z^2}$ . The mean density profile is computed from a Crocco-Busemann relation:

$$\rho(r) = \rho_j \left( 1 + \frac{\gamma - 1}{2} M^2 \frac{u(r)}{u_j} \left( 1 - \frac{u(r)}{u_j} \right) \right)^{-1} \quad (39)$$

544 The azimuthal and radial velocities are initially null, and the pressure is equal to  $p_0$ . In order to seed  
 545 the laminar-turbulent transition of the jet flow, vortex rings are added to the flow field in the shear  
 546 layer at  $x = r = r_0$ , at each time step of the computation [34]. The amplitude of the perturbations  
 547 is equal to  $\alpha = 0.007$  and the half-width of the Gaussian profile that defines the vortices is equal to  
 548  $\Delta_0 = 0.045r_0$ . The small disturbances are divergence-free to minimize the production of spurious  
 549 acoustic waves.

## 550 7.2. Numerical set-up

551 Two simulations are carried out using Cartesian grids with and without a non-conforming interface.  
 552 The computational domain extends from  $x = 0$  up to  $x = 48r_0$  in the flow direction and from 0 up  
 553 to  $20r_0$  in the  $y$  and  $z$  directions.

554 The spatial discretization in the grid without a non-conforming interface is presented in Fig. 20.  
 555 In the  $x$  direction, for  $0 \leq x \leq 25r_0$ , the axial mesh spacing is constant with  $\Delta x = 0.1r_0$ , and then  
 556 increases with a rate of 0.4% up to  $x = 35r_0$ , and with a rate of 8% for  $x > 35r_0$ . In the  $y$  and  $z$   
 557 directions, the mesh is finer than in the  $x$  direction in order to resolve the shear layers. The grid  
 558 spacing does not vary for  $y, z \leq r_0$ , with  $\Delta y = \Delta z = r_0/30$ . For  $y, z > r_0$ , a stretching ratio of 2%  
 559 is applied up to  $r = 20r_0$ .

560 The non-conforming mesh is built from the conforming mesh. Figure 21 provides a simplified  
 561 representation of the two meshes in the  $x$ - $y$  plane, with the non-conforming interface indicated  
 562 by a bold line in Fig. 21(b). In the jet flow region, for  $x \leq 14r_0$ , the two meshes are identical.

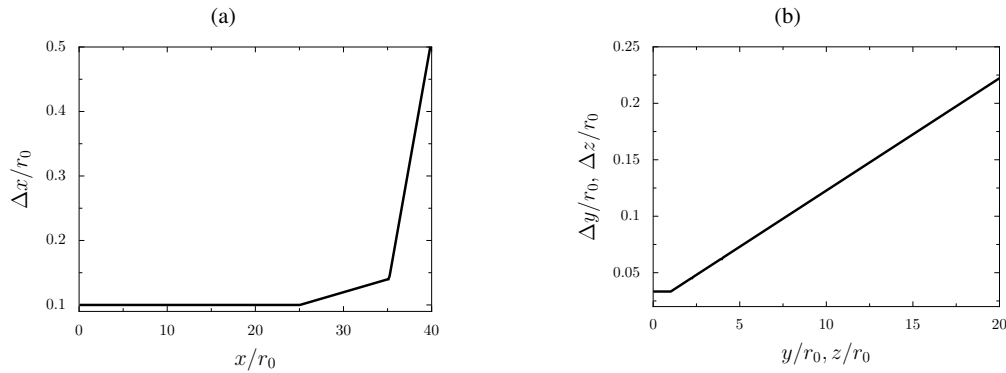


Figure 20. Representation of the spatial discretizations in the conforming grid: (a) axial discretization and (b) discretization in the  $y$  and  $z$  directions.

563 Downstream of the end of the jet potential core expected to be around  $x_p \simeq 10r_0$  according to  
 564 reference [35], a non-conforming interface is defined at  $x = 14r_0$ , as shown in Fig. 21(b). The  
 565 location of the interface is chosen downstream of the jet sound source region, which is found for  
 566  $x \leq x_p$ . For  $x > 14r_0$ , the very fine mesh spacings used in the  $y$  and  $z$  directions at the jet inlet to  
 567 discretize the jet shear layers are not necessary due to the jet spreading. Therefore, downstream of  
 568 the interface, the grid spacings  $\Delta y$  and  $\Delta z$  in the non-conforming mesh are twice as coarse as in the  
 569 conforming grid. Thus, the number of mesh points in the non-conforming grid, equal to 42 million  
 570 points, is reduced by 44% compared to the conforming grid.

571 The conforming grid used in the present work is finer than the one used in the reference [33] by  
 572 factors of 1.3 and 2 in the axial and radial directions respectively. In addition, since the resolutions  
 573 of the two grids used in this study differ for  $x > 14r_0$ , small differences between the results from the  
 574 two simulations are expected, as demonstrated by the grid sensitivity of turbulent jet flows presented  
 in reference [36].

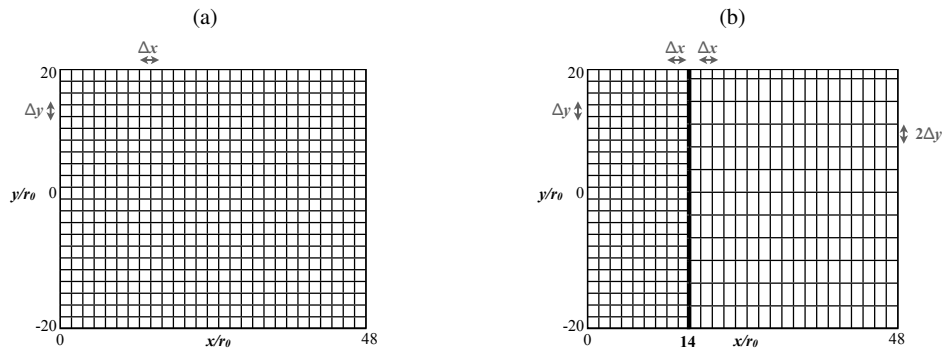


Figure 21. Sketch of (a) the conforming grid and (b) the non-conforming grid in the  $x$ - $y$  plane.

575

576 In each computation, the jet flow is simulated over a time period  $T = 2 \times 10^5 \Delta t = 2000r_0/c_0$ .  
 577 The flow initialization lasts over  $600r_0/c_0$ . The velocity and pressure fields are then recorded during  
 578 a sampling period  $T_s = 1400r_0/c_0$ , leading to a minimum Strouhal number  $St_{\min} = D/(T_s u_j)$  of  
 579  $1.6 \times 10^{-3}$ . In order to study the development of the jet flow, the velocity field is recorded along  
 580 the jet axis and at  $r = r_0$ . In order to examine the acoustic sound radiated in the near-field region,  
 581 pressure spectra at  $r = 8r_0$  are computed by averaging over 8 points equally distributed on circles

582 centered on the jet axis. The data are sampled every 10 time steps in order to compute spectra up to a  
 583 maximum Strouhal number  $St_{\max} = fD/u_j = 5.55$ , and the spectra are evaluated from overlapping  
 584 samples of duration  $93.3r_0/c_0$ .

585 At the non-conforming interface, the flux reconstruction for plane interfaces presented in  
 586 section 3.1 is applied. The RBF interpolations are performed using  $n_v = 8$  points and second-  
 587 degree polynomial functions. The choice of the values of  $n_v$  and  $\text{deg}(P)$  is motivated by the fact  
 588 that it provided accurate results for an acoustic pulse propagation and for a vortex convection on  
 589 non-conforming Cartesian grids in two-dimensional problems (see sections 5 and 6.1).

590 *7.3. Results*

591 Snapshots of the vorticity magnitude and the fluctuating pressure obtained in the two simulations  
 592 are presented in Fig. 22. The non-conforming interface at  $x = 14r_0$  is indicated by a vertical line  
 593 in Fig. 22(b). In the two simulations, the jet mixing layers are found to develop from  $x = r_0$  and  
 594 to interact around  $x = 12r_0$ . Farther downstream, in Fig. 22(b), vortical structures cross the non-  
 595 conforming interface and display lower levels than those located upstream for  $x < 14r_0$ . These  
 596 levels are also lower than those obtained for  $x > 14r_0$  in Fig. 22(a). This is most likely due to  
 597 the mesh resolution that is twice as coarse in the  $y$  direction for  $x > 14r_0$  in the non-conforming  
 598 grid [36]. In the pressure field, acoustic waves propagate from the jet with an angle of about  $30^\circ$   
 599 relative to the  $x$ -axis. In Fig. 22(b), no discontinuity of the pressure waves radiated from the jet and  
 600 no spurious reflection are visible in the vicinity of the non-conforming interface.

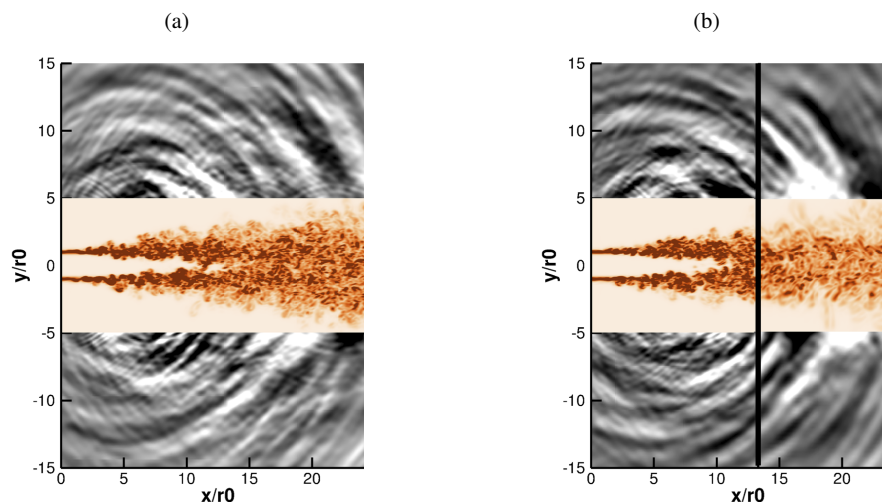


Figure 22. Snapshots in the  $x$ - $y$  plane of the vorticity modulus in the flow and of the fluctuating pressure outside obtained from the simulations using (a) a conforming grid and (b) a non-conforming grid. The color scale is from 0 to  $2.5u_j/r_0$  for the vorticity and the grey scale is from -70 to 70 Pa for the pressure.

601 More quantitative results are shown in Fig. 23, where the mean axial velocity profiles obtained in  
 602 the two simulations are given along the jet axis and at  $r = r_0$ . In Fig. 23(a), the two profiles along  
 603 the jet axis are superimposed for  $x \leq 20r_0$ . They indicate that in both jets, the jet potential core ends  
 604 at  $x_p = 12r_0$ . For  $x > 20r_0$ , slightly lower velocity values are found using the non-conforming grid,  
 605 with differences that do not exceed  $0.025u_j$ . In Fig. 23(b), the velocity profiles at  $r = r_0$  are also

606 superimposed upstream of the grid interface, whereas velocity is lower by  $0.02u_j$  for  $x > 14r_0$  in  
 607 the simulation using a non-conforming grid.

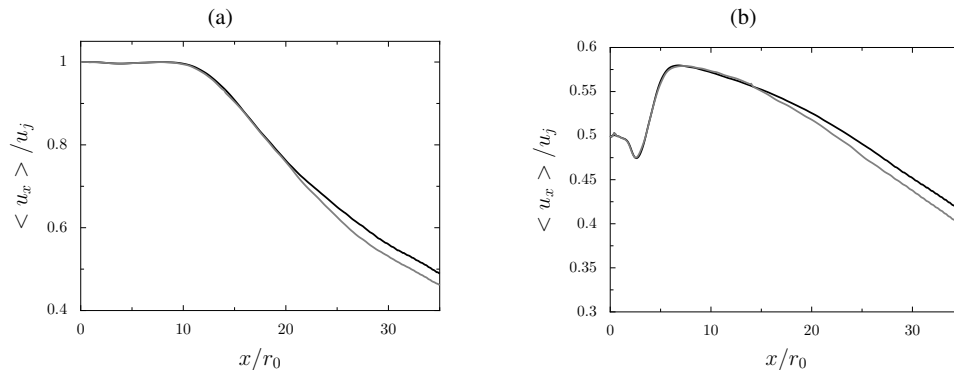


Figure 23. Representation of the mean axial velocity (a) along the jet centerline and (b) at  $r = r_0$ : simulations with — a conforming grid and — a non-conforming grid.

608 The rms axial and radial velocities  $\langle u'_x u'_x \rangle^{1/2} / u_j$  and  $\langle u'_r u'_r \rangle^{1/2} / u_j$  calculated at  $r = r_0$   
 609 are represented in Fig. 24, where the prime stands for the fluctuating quantity and  $\langle \cdot \rangle$  for time  
 610 average. In Fig. 24(a) and 24(b), in the same way as for the mean profiles of Fig. 23(b), the  
 611 profiles from the two simulations are identical for  $x < 14r_0$ , with the same peaks of turbulence.  
 612 For  $x \geq 14r_0$ , small differences of less than 1% appear between the two computations. In particular,  
 613 using a non-conforming grid, the rms profiles slightly decrease at the non-conforming interface  
 614  $x = 14r_0$  and present a small hump downstream for  $17r_0 \leq x \leq 27r_0$ . Despite this, for  $x \geq 27r_0$ ,  
 615 very similar turbulent levels are found in the two simulations. The small differences reported  
 616 between the two simulations in Fig. 23 and 24 are likely due to the resolution of the non-conforming  
 617 grid that is coarser for  $x \geq 14r_0$  [36].

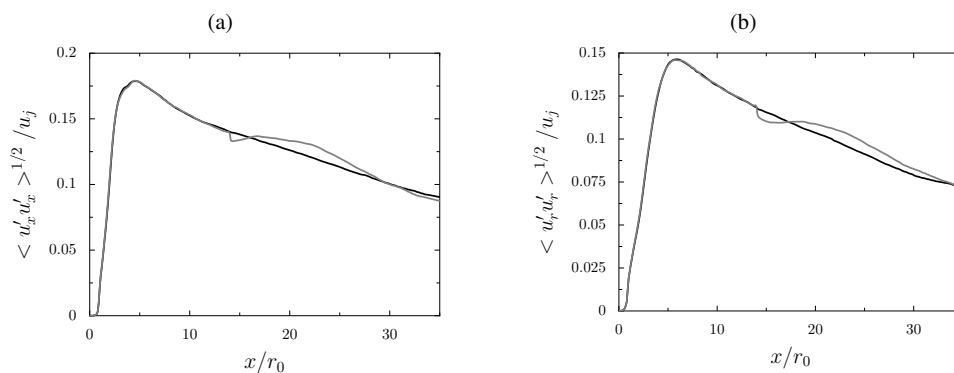


Figure 24. Representation of the (a) axial and (b) radial rms velocity profiles at  $r = r_0$ : simulations with — a conforming grid and — a non-conforming grid.

618 In order to investigate the effects of the presence of the non-conforming interface on the jet  
 619 flow features, axial velocity spectra are computed at three locations along the jet axis, upstream  
 620 of the non-conforming interface at  $x = 13.4r_0$ , and downstream of the interface at  $x = 14.7r_0$   
 621 and at  $x = 20r_0$ . The spectra are represented in Fig. 25 as a function of the Strouhal number.  
 622 At  $x = 13.4r_0$ , the spectra exhibit similar shapes and levels, which suggests that the jet flow  
 623 components are not affected by the close proximity of the non-conforming interface. Downstream

624 of the interface, at  $x = 14.7r_0$ , the spectra from the two simulations show similar levels for  $St < 2$   
 625 whereas a more pronounced decrease is observed for  $St \geq 2$  for the spectrum obtained using the  
 626 non-conforming grid. At  $x = 20r_0$ , the spectrum from the non-conforming grid displays slightly  
 627 higher levels at low Strouhal numbers and collapses more rapidly for  $St \geq 2$ . The origin of the  
 628 small differences observed here does not seem to be related to the presence of the non-conforming  
 629 interface but to a poorer discretization of the jet coherent structures using the non-conforming  
 630 mesh [36].

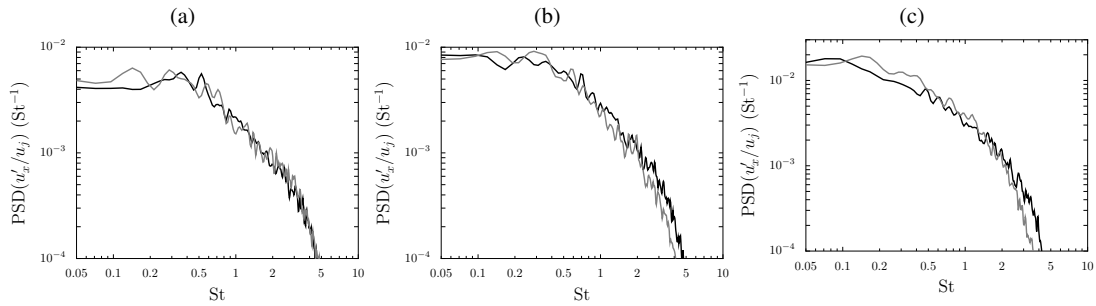


Figure 25. Representation of the axial velocity spectra on the jet axis (a) upstream of the grid interface at  $x = 13.4r_0$ , and downstream at (b)  $x = 14.7r_0$  and (c)  $x = 20r_0$ : — conforming grid and - - - non-conforming grid.

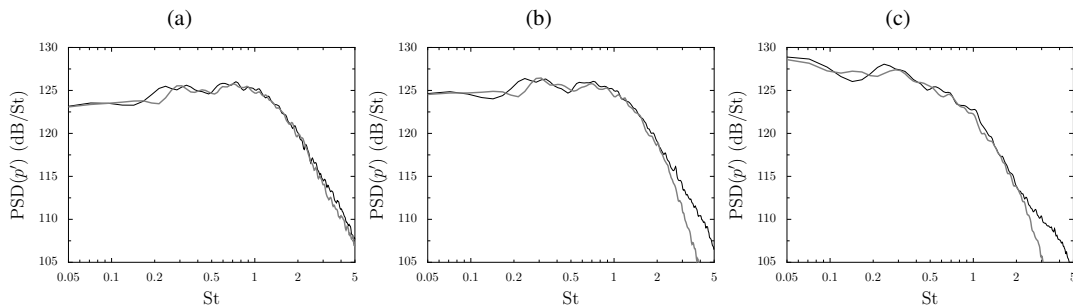


Figure 26. Representation of the pressure spectra at  $r = 8r_0$  (a) upstream of the grid interface at  $x = 13.4r_0$ , and downstream at (b)  $x = 14.7r_0$  and (c)  $x = 20r_0$ : — conforming grid and - - - non-conforming grid.

631 Finally, to examine the acoustic results in the near-field region, pressure spectra at  $r = 8r_0$  are  
 632 plotted in Fig. 26 for the axial positions  $x = 13.4r_0$ ,  $x = 14.7r_0$  and  $x = 20r_0$ . The spectra at the  
 633 three locations display broadband shapes, which is typical of subsonic turbulent jet noise [37].  
 634 Upstream of the grid interface, at  $x = 13.4r_0$ , the spectra from the two simulations are very similar,  
 635 which is expected since the two meshes are identical for  $x \leq 14r_0$ . Downstream of the interface,  
 636 at  $x = 14.7r_0$  and  $x = 20r_0$ , the acoustic spectra predicted by the two simulations are in good  
 637 agreement for Strouhal numbers  $St < 2$ . For  $St \geq 2$ , the spectrum obtained from the non-conforming  
 638 grid collapses more rapidly. This drop is due to the lower mesh cut-off Strouhal number in that  
 639 case. Indeed, at  $r = 8r_0$ , considering that the spatial schemes resolve wavelengths discretized by at  
 640 least 5 points [14], the cut-off Strouhal number is of  $St_{\text{cut-off}} = 2$  for the non-conforming grid and of  
 641  $St_{\text{cut-off}} = 4$  for the conforming grid.

642 These results demonstrate that the present non-conforming grid methodology can be used in order  
643 to reduce the size of the mesh and thus the computational cost, without appreciably biasing the jet  
644 development and the noise field radiated by the jet.

## 8. CONCLUSION

645 In this study, a flux reconstruction technique is presented in order to perform aeroacoustic  
646 computations using high-order finite-volume spatial schemes on structured meshes including non-  
647 conforming grid interfaces. The spatial discretization is carried out using a sixth-order implicit  
648 scheme in combination with a sixth-order implicit selective filter. The flux reconstruction can  
649 be applied to plane or curved non-conforming interfaces. It is performed using non-centered  
650 formulations for the spatial scheme and the selective filter at the non-conforming interface. These  
651 formulations require the definition of ghost cells and ghost interfaces. The flow variables in the  
652 ghost cells and at the interfaces are computed using meshless interpolations with radial basis  
653 functions. For computational efficiency, all the interpolation coefficients are computed once in the  
654 beginning of the simulation and then stored in memory. The properties of the RBF interpolations  
655 in the wavenumber space are studied. The accuracy of the flux reconstruction is evaluated for an  
656 acoustic pulse introduced in the vicinity of a non-conforming interface using 2-D Cartesian grids.  
657 RBF interpolations using  $n_v = 8$  points in conjunction with a 2nd-degree polynomial function are  
658 found to be sufficient to obtain accurate results. The performance of the flux reconstruction is  
659 then examined for the convection of a vortex using 2-D Cartesian and wavy grids. The results  
660 on Cartesian grids highlight the benefits of using RBF interpolations, instead of a low-order flux  
661 reconstruction, in order to reduce the spurious pressure waves produced at the block interface. The  
662 results obtained with different spatial resolutions also show that the non-conforming grids must  
663 be designed such that the flow field is well discretized by the mesh before and after the grid  
664 interface. The results of the computations performed on wavy grids demonstrate the advantages  
665 of using the flux reconstruction for curved interfaces. More precisely, the flux reconstruction  
666 technique designed for curved interfaces produces lower spurious noise level than those obtained  
667 using the reconstruction for plane interfaces. It seems also recommended to use low curvature  
668 non-conforming interfaces. Finally, the application of the flux reconstruction technique to 3-D  
669 flows is illustrated for a turbulent round jet flow at a diameter-based Reynolds number of  $4 \times 10^5$ .  
670 Simulations are performed with and without a non-conforming grid interface downstream of the jet  
671 potential core. The jet development is only slightly affected by the presence of the non-conforming  
672 grids, and the acoustic spectra in the near-field region are very similar.

## ACKNOWLEDGMENTS

673 This study, financially supported by Airbus, was performed at CERFACS in the context of the  
674 PhD thesis of the first author. The authors gratefully acknowledge Dr. Marc Montagnac for his  
675 crucial help in the development of the numerical code used in this work. The post-processing of the  
676 numerical results is carried out using Antares (release 1.11.0, <https://www.cerfacs.fr/antares>) [38].

APPENDIX

A. CALCULATION OF RBF INTERPOLATION COEFFICIENTS

677 *A.1. Interpolation of the flow variables in the ghost cells*

678 As presented in section 3.1.3, in order to reconstruct the flow variables in the ghost cells, RBF  
 679 interpolations are performed. A RBF interpolation  $u_{\text{RBF}}$  of the variable  $u$  at point  $\mathbf{x}$  is defined as a  
 680 linear combination of Wendland’s radial basis functions  $\Phi$  and a polynomial term:

$$u_{\text{RBF}}(\mathbf{x}) = \sum_{j=1}^{n_v} \xi_j \Phi(\mathbf{x}, \mathbf{x}_j) + \sum_{q=1}^m \zeta_q P_q(\mathbf{x}) \quad (40)$$

681 where  $\xi_j$  and  $\zeta_q$  are the unknown interpolation coefficients. In this study,  $C^2$  Wendland’s basis  
 682 functions [9, 28] with compact support are used:

$$\Phi(\mathbf{x}, \mathbf{x}_j) = \Phi(r_j) = \left(1 - \frac{r_j}{R_v}\right)_+^4 \left(4 \frac{r_j}{R_v} + 1\right) \quad 1 \leq j \leq n_v \quad (41)$$

683 where  $r_j$  is the Euclidian distance between the points  $\mathbf{x}$  and  $\mathbf{x}_j$ ,  $(1 - \frac{r_j}{R})_+$  is defined by:

$$\left(1 - \frac{r_j}{R_v}\right)_+ = \begin{cases} \left(1 - \frac{r_j}{R_v}\right) & \text{if } 0 \leq r_j \leq R_v \\ 0 & \text{if } r_j > R_v \end{cases} \quad (42)$$

684 and  $R_v$  is the radius of the circle of center  $\mathbf{x}$  defined such that  $R_v = Ar_{\min}$ , with  
 685  $r_{\min} = \min(r_j)_{(j=1, \dots, n_v)}$  and  $A$  is a value chosen such that  $n_v$  cells are contained inside the circle.  
 686 A representation of the ghost cell and the  $n_v$  cells is provided in Fig. 27.

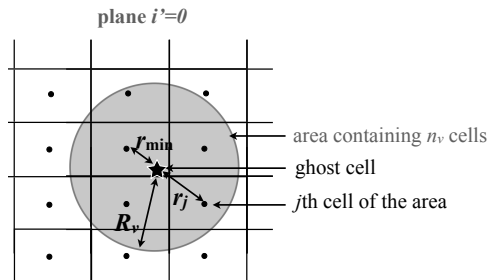


Figure 27. Representation of the cloud of  $n_v$  cells used for the interpolation of the flow variables in the ghost cell. The center of the ghost cell is indicated by a star.

687 The values of  $\xi_j$  and  $\zeta_q$  are determined so that the approximation  $u_{\text{RBF}}(\mathbf{x})$  is exact for all the  $n_v$   
 688 points. Therefore, the interpolation formulation (40) satisfies the following relations:

$$u_{\text{RBF}}(\mathbf{x}_k) = u_k = \sum_{j=1}^{n_v} \xi_j \Phi(\mathbf{x}_k, \mathbf{x}_j) + \sum_{q=1}^m \zeta_q P_q(\mathbf{x}_k) \quad \text{for } 1 \leq k \leq n_v \quad (43)$$

689 where  $(u_k)_{k=1, \dots, n_v}$  are the values of  $u$  known in the  $n_v$  cells considered for the interpolation. In  
 690 order to ensure that approximation (40) has a unique solution [18, 29], the following orthogonality



691 constraints are imposed:

$$\sum_{j=1}^{n_v} P_q(\mathbf{x}_j) \xi_j = 0 \quad \text{for } 1 \leq q \leq m \quad (44)$$

692 Therefore, the values of  $\xi_j$  and  $\zeta_q$  are computed by resolving the linear system:

$$\mathbf{M} \begin{pmatrix} \boldsymbol{\xi} \\ \boldsymbol{\zeta} \end{pmatrix} = \begin{pmatrix} \boldsymbol{\Phi} & \mathbf{P} \\ \mathbf{P}^T & \mathbf{0} \end{pmatrix} \begin{pmatrix} \boldsymbol{\xi} \\ \boldsymbol{\zeta} \end{pmatrix} = \begin{pmatrix} \mathbf{u}^{\text{set}} \\ \mathbf{0} \end{pmatrix} \quad (45)$$

693 where  $\boldsymbol{\xi} = (\xi_1, \dots, \xi_{n_v})^T$  and  $\boldsymbol{\zeta} = (\zeta_1, \dots, \zeta_m)^T$  are the vectors of the interpolation coefficients to be  
694 determined,  $\mathbf{u}^{\text{set}} = (u_1, \dots, u_{n_v})^T$ , and  $\boldsymbol{\Phi} \in \mathbb{R}^{n_v \times n_v}$  and  $\mathbf{P} \in \mathbb{R}^{n_v \times m}$  are the matrices defined by:

$$\begin{aligned} \Phi_{kj} &= \Phi(\mathbf{x}_k, \mathbf{x}_j) \quad \text{for } 1 \leq k, j \leq n_v \\ \mathbf{P}_{kq} &= P_q(\mathbf{x}_k) \quad \text{for } 1 \leq k \leq n_v \text{ and } 1 \leq q \leq m \end{aligned} \quad (46)$$

695 The solution of the system (45) writes:

$$\begin{pmatrix} \boldsymbol{\xi} \\ \boldsymbol{\zeta} \end{pmatrix} = \mathbf{M}^{-1} \begin{pmatrix} \mathbf{u}^{\text{set}} \\ \mathbf{0} \end{pmatrix} = \begin{pmatrix} \sum_{k=1}^{n_v} m_{1,k} u_k \\ \vdots \\ \vdots \\ \sum_{k=1}^{n_v} m_{n_v+m,k} u_k \end{pmatrix} \quad (47)$$

696 where  $m_{i,j}$  are the coefficients of the matrix  $\mathbf{M}^{-1}$ . Introducing Eq. (47) in Eq. (40), the RBF  
697 interpolation applied to a ghost cell of center  $\mathbf{x}_{\text{ghost}}$  is given by the relation:

$$u_{\text{RBF}}(\mathbf{x}_{\text{ghost}}) = \sum_{k=1}^{n_v} \Psi_k(\mathbf{x}_{\text{ghost}}) u_k \quad (48)$$

698 where the coefficients  $\Psi_k(\mathbf{x}_{\text{ghost}})$  are defined as:

$$\Psi_k(\mathbf{x}_{\text{ghost}}) = \sum_{j=1}^{n_v} m_{j,k} \Phi(\mathbf{x}_{\text{ghost}}, \mathbf{x}_j) + \sum_{q=1}^m m_{n_v+q,k} P_q(\mathbf{x}_{\text{ghost}}) \quad (49)$$

699 Note that the  $n_v$  coefficients  $\Psi_k(\mathbf{x}_{\text{ghost}})$  are independent of the flow variables. Therefore, they are  
700 computed and stored in memory at the beginning of the simulation. The interpolation is therefore  
701 performed at a low CPU cost since the value of  $u_{\text{RBF}}$  is simply obtained from the sum (48).

## 702 A.2. Interpolation of the flow variables at the non-conforming grid interface

703 A.2.1. Plane interfaces As described in section 3.1.3, the interpolation formulation at the block  
704 interface writes:

$$\begin{aligned} \tilde{u}_{L'} &= \frac{1}{|I'_L|} \int_{I'_L} u_{\text{RBF}}(\mathbf{x}) \, d\mathbf{x} \\ &= \sum_{j'=1}^{n_v} \tilde{\xi}_{j'} \left( \frac{1}{|I'_L|} \int_{I'_L} \Phi(\mathbf{x}, \mathbf{x}_{j'}) \, d\mathbf{x} \right) + \sum_{q=1}^m \tilde{\zeta}_q \left( \frac{1}{|I'_L|} \int_{I'_L} P_q(\mathbf{x}) \, d\mathbf{x} \right) \end{aligned} \quad (50)$$

705 The interpolation coefficients  $\tilde{\xi}_{j'}$  and  $\tilde{\zeta}_q$  are determined by integrating Eq. (40) on the  $n_v$  interfaces  
 706  $(I_{R,1}, \dots, I_{R,j'}, I_{R,j'+1}, \dots, I_{R,n_v})$  of Fig. 5(c), and by imposing that the integrals obtained are equal  
 707 to the component  $\tilde{u}$  of vectors  $(\tilde{\mathbf{U}}_{R,1}, \dots, \tilde{\mathbf{U}}_{R,j'}, \dots, \tilde{\mathbf{U}}_{R,n_v})$  of block R. It yields for the interface  $I_{R,k}$ :

$$\tilde{u}_{R,k} = \sum_{j'=1}^{n_v} \tilde{\xi}_{j'} \left( \frac{1}{|I_{R,k}|} \int_{I_{R,k}} \Phi(\mathbf{x}, \mathbf{x}_{j'}) \, d\mathbf{x} \right) + \sum_{q=1}^m \tilde{\beta}_q \left( \frac{1}{|I_{R,k}|} \int_{I_{R,k}} P_q(\mathbf{x}) \, d\mathbf{x} \right) \quad \text{for } 1 \leq k \leq n_v \quad (51)$$

708

709 where  $\tilde{u}_{R,k}$  is a component of the averaged field  $\tilde{\mathbf{U}}_{R,k}$  at the interface  $I_{R,k}$ . In practice, the  
 710 coefficients  $\tilde{\xi}_{j'}$  and  $\tilde{\zeta}_q$  are estimated by solving the linear system:

$$\begin{pmatrix} \tilde{\Phi} & \tilde{\mathbf{P}} \\ \tilde{\mathbf{P}}^T & \mathbf{0} \end{pmatrix} \begin{pmatrix} \tilde{\xi} \\ \tilde{\zeta} \end{pmatrix} = \begin{pmatrix} \tilde{\mathbf{u}}^{\text{set}} \\ \mathbf{0} \end{pmatrix} \quad (52)$$

711

712 where  $\tilde{\xi} = (\tilde{\xi}_1, \dots, \tilde{\xi}_{n_v})^T$  and  $\tilde{\zeta} = (\tilde{\zeta}_1, \dots, \tilde{\zeta}_m)^T$  are the vectors of the interpolation coefficients,  
 713  $\tilde{\mathbf{u}}^{\text{set}} = (\tilde{u}_{R,1}, \dots, \tilde{u}_{R,n_v})^T$ , and  $\tilde{\Phi} \in \mathbb{R}^{n_v \times n_v}$  and  $\tilde{\mathbf{P}} \in \mathbb{R}^{n_v \times m}$  are the matrices defined by:

$$\begin{aligned} \tilde{\Phi}_{kj'} &= \frac{1}{|I_{R,k}|} \int_{I_{R,k}} \Phi(\mathbf{x}, \mathbf{x}_{j'}) \, d\mathbf{x} \quad \text{for } 1 \leq k, j' \leq n_v \\ \tilde{\mathbf{P}}_{kq} &= \frac{1}{|I_{R,k}|} \int_{I_{R,k}} P_q(\mathbf{x}) \, d\mathbf{x} \quad \text{for } 1 \leq k \leq n_v \text{ and } 1 \leq q \leq m \end{aligned} \quad (53)$$

714 As in section A.1, the RBF interpolation (50) can be reformulated as:

$$\tilde{u}_{L'} = \sum_{k=1}^{n_v} \tilde{\Psi}_k u_k \quad (54)$$

715 where the coefficients  $\tilde{\Psi}_k$  are defined as:

$$\tilde{\Psi}_k = \sum_{j'=1}^{n_v} \frac{1}{|I'_L|} \int_{I'_L} m'_{j',k} \Phi(\mathbf{x}, \mathbf{x}_{j'}) \, d\mathbf{x} + \sum_{q=1}^m m'_{n_v+q,k} \frac{1}{|I'_L|} \int_{I'_L} P_q(\mathbf{x}) \, d\mathbf{x} \quad (55)$$

716 where  $m'_{i,j}$  are the coefficients of the inverse of the matrix of the system (52). In practice, the values  
 717 of  $\tilde{\Psi}_k$  are computed only once and then stored in memory at the beginning of the simulation.

718 *A.2.2. Curved interfaces* In order to take into account the curvature effect of grid interfaces, the  
 719 interface  $I'_{L_{\text{curved}}}$  is defined by the function  $\sigma$ . The interpolation formulation to compute the flow  
 720 component  $u$  at the interface  $I'_{L_{\text{curved}}}$  writes, as in Eq. (50):

$$\begin{aligned} \tilde{u}_{L'} &= \frac{1}{|I'_{L_{\text{curved}}}|} \int_{I'_{L_{\text{curved}}}} u_{\text{RBF}}(\mathbf{x}) \, d\mathbf{x} \\ &= \sum_{j'=1}^{n_v} \tilde{\xi}_{j'} \left( \frac{1}{|I'_{L_{\text{curved}}}|} \int_{I'_{L_{\text{curved}}}} \Phi(\mathbf{x}, \mathbf{x}_{j'}) \, d\mathbf{x} \right) + \sum_{q=1}^m \tilde{\zeta}_q \left( \frac{1}{|I'_{L_{\text{curved}}}|} \int_{I'_{L_{\text{curved}}}} P_q(\mathbf{x}) \, d\mathbf{x} \right) \end{aligned} \quad (56)$$

721 The interpolation coefficients  $\tilde{\xi}_{j'}$  and  $\tilde{\zeta}_q$  are calculated by integrating Eq. (40) on the  $n_v$  interfaces  
 722  $(I_{R,1_{\text{curved}}}, \dots, I_{R,j'_{\text{curved}}}, I_{R,j'+1_{\text{curved}}}, \dots, I_{R,n_v_{\text{curved}}})$  also defined by the function  $\sigma$ , and by imposing  
 723 that the integrals thus obtained are equal to the component  $\tilde{u}$  of vectors  $(\tilde{\mathbf{U}}_{R,1}, \dots, \tilde{\mathbf{U}}_{R,j'}, \dots, \tilde{\mathbf{U}}_{R,n_v})$   
 724 of block R. It yields for the interface  $I_{R,k_{\text{curved}}}$ :

$$\tilde{u}_{R,k} = \sum_{j'=1}^{n_v} \tilde{\xi}_{j'} \left( \frac{1}{|I_{R,k_{\text{curved}}}|} \int_{I_{R,k_{\text{curved}}}} \Phi(\mathbf{x}, \mathbf{x}_{j'}) \, d\mathbf{x} \right) + \sum_{q=1}^m \tilde{\zeta}_q \left( \frac{1}{|I_{R,k_{\text{curved}}}|} \int_{I_{R,k_{\text{curved}}}} P_q(\mathbf{x}) \, d\mathbf{x} \right) \quad \text{for } 1 \leq k \leq n_v \quad (57)$$

725

726 where  $\tilde{u}_{R,k}$  is a component of the averaged field  $\tilde{\mathbf{U}}_{R,k}$  at the interface  $I_{R,k_{\text{curved}}}$ . The coefficients  $\tilde{\xi}_{j'}$   
 727 and  $\tilde{\zeta}_q$  are then computed from the resolution of a linear system similar to (52).

728

### 729 *A.3. Flux reconstruction without RBF interpolation*

730 The technique of flux reconstruction without RBF interpolation is identical to the technique  
 731 presented in section 3, except for the calculation of the flow variables in the ghost cells and at  
 732 the grid interfaces which is performed using 2nd-order interpolations.

733 *A.3.1. Interpolation for ghost cells* The interpolation technique is described for the calculation of  
 734 the flow variables  $\mathbf{U}$  in the ghost cell located at  $(i' = 0, j)$  in Fig. 5(a). For this purpose, as shown  
 735 in Fig. 28, the interface  $I_L$  in blue is divided in two parts  $I_{\text{AM}}$  and  $I_{\text{MB}}$ . The interface  $I_{\text{AM}}$  is the  
 736 intersection between the interfaces  $I_L$  and  $I_{R,j'}$ , and the interface  $I_{\text{MB}}$  is the intersection between  
 737 the interfaces  $I_L$  and  $I_{R,j'+1}$ . The value of  $\mathbf{U}$  in the ghost cell is determined as the weighted sum of  
 738  $\mathbf{U}$  in the cells  $(i' = 0, j')$  and  $(i' = 0, j' + 1)$  in block R:

$$\mathbf{U}_{i'=0,j} = \frac{S_{\text{AM}}}{S_{\text{AB}}} \mathbf{U}_{i'=0,j'} + \frac{S_{\text{BM}}}{S_{\text{AB}}} \mathbf{U}_{i'=0,j'+1} \quad (58)$$

739 where  $S_k$  is the surface of interface  $I_k$ . Similarly, the value of  $\mathbf{U}$  in the second ghost cell in Fig. 5(a)  
 740 is calculated as the weighted sum of  $\mathbf{U}$  in the cells  $(i' = 1, j')$  and  $(i' = 1, j' + 1)$ .

741 *A.3.2. Interpolation at the grid interface* In order to compute the convective flux at the non-  
 742 conforming interface, the value of the vector  $\tilde{\mathbf{U}}$  at the ghost interface  $I'_L$  in block R is computed

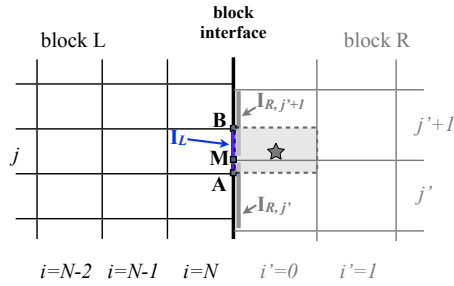


Figure 28. Representation of a non-conforming grid where the interface  $I_L$  is divided in two interfaces  $I_{AM}$  and  $I_{MB}$ . The flow variables in the ghost cell indicated in grey are computed as a weighted sum of the flow variables in cells  $(i' = 0, j')$  and  $(i' = 0, j' + 1)$ .

743 as the weighted sum:

$$\tilde{\mathbf{U}}'_L = \frac{S_{AM}}{S_{AB}} \tilde{\mathbf{U}}_{R,j'} + \frac{S_{BM}}{S_{AB}} \tilde{\mathbf{U}}_{R,j'+1} \quad (59)$$

744 where the values of  $\tilde{\mathbf{U}}$  at the interfaces  $I_{R,j'}$  and  $I_{R,j'+1}$  are computed from the upwind scheme (14).  
745 The value of  $\tilde{\mathbf{U}}$  at the interface  $I_L$  is calculated from the upwind scheme (13). Finally, the convective  
746 flux at the block interface is determined from the values of  $\tilde{\mathbf{U}}_L$  and  $\tilde{\mathbf{U}}'_L$  by resolving a Riemann flux  
747 problem [25].

#### REFERENCES

- 748  
749
- 750 1. C Bailly, C Bogey, and O Marsden. Progress in direct noise computation. *International Journal of Aeroacoustics*,  
751 9(1-2):123–143, 2010.
  - 752 2. C Bogey and C Bailly. A family of low dispersive and low dissipative explicit schemes for flow and noise  
753 computations. *Journal of Computational Physics*, 194(1):194–214, 2004.
  - 754 3. T Colonius and SK Lele. Computational aeroacoustics: progress on nonlinear problems of sound generation.  
755 *Progress in Aerospace Sciences*, 40(6):345–416, 2004.
  - 756 4. C Bogey, O Marsden, and C Bailly. Large-eddy simulation of the flow and acoustic fields of a Reynolds number  
757  $10^5$  subsonic jet with tripped exit boundary layers. *Physics of Fluids*, 23:035104, 2011.
  - 758 5. C Bogey and C Bailly. Influence of nozzle-exit boundary-layer conditions on the flow and acoustic fields of initially  
759 laminar jets. *Journal of Fluid Mechanics*, 663:507–538, 2010.
  - 760 6. GA Brès, P Jordan, T Colonius, M Le Rallic, V Jaunet, and SK Lele. Large eddy simulation of a Mach 0.9 turbulent  
761 jets. *Proceedings of the Summer Program*, pages 221–230, 2014.
  - 762 7. D Desvigne, O Marsden, C Bogey, and C Bailly. Development of noncentered wavenumber-based optimized  
763 interpolation schemes with amplification control for overlapping grids. *SIAM Journal on Scientific Computing*,  
764 32(4):2074–2098, 2010.
  - 765 8. J Huber, G Drochon, A Pintado-Peno, F Cléro, and G Bodard. Large-Scale Jet Noise Testing, Reduction and  
766 Methods validation "EXEJET": 1. Project Overview and Focus on Installation. *20th AIAA/CEAS Aeroacoustics  
767 Conference, paper AIAA-2014-3032*, 2014.
  - 768 9. WJ Costin and CB Allen. Numerical study of radial basis function interpolation for data transfer across  
769 discontinuous mesh interfaces. *International Journal for Numerical Methods in Fluids*, 72(10):1076–1095, 2013.
  - 770 10. CKW Tam and JC Webb. Dispersion-relation-preserving finite difference schemes for computational acoustics.  
771 *Journal of Computational Physics*, 107:262–281, 1993.
  - 772 11. SK Lele. Compact finite difference schemes with spectral-like resolution. *Journal of Computational Physics*,  
773 103:16–42, 1992.
  - 774 12. F Fosso Pouangué, H Deniau, F Sicot, and P Sagaut. Curvilinear finite volume scheme using high order compact  
775 interpolation. *Journal of Computational Physics*, 229(13):5090–5122, 2010.
  - 776 13. MR Visbal and DV Gaitonde. On the use of higher-order finite-difference schemes on curvilinear and deforming  
777 meshes. *Journal of Computational Physics*, 181:155–185, 2002.

- 778 14. A Fosso Pouangué, M Sanjosé, S Moreau, G Daviller, and H Deniau. Subsonic jet noise simulations using both  
779 structured and unstructured grids. *AIAA Journal*, 53(1):55–69, 2014.
- 780 15. R Biolchini, C Bailly, J-F Boussuge, and R Fernando. Numerical study on the relation between hydrodynamic  
781 fluctuations and noise in hot jets at high Reynolds numbers. In *22nd AIAA/CEAS Aeroacoustics Conference, paper*  
782 *AIAA-2016-3048*, 2016.
- 783 16. P Grenson and H Deniau. Large-eddy simulation of an impinging heated jet for a small nozzle-to-plate distance  
784 and high Reynolds number. *International Journal of Heat and Fluid Flow*, 68:348–363, 2017.
- 785 17. CP Arroyo, G Daviller, G Puigt, C Airiau, and S Moreau. Identification of temporal and spatial signatures of  
786 broadband shock-associated noise. *Shock Waves*, pages 1–18, 2018.
- 787 18. JG Wang and GR Liu. A point interpolation meshless method based on radial basis functions. *International Journal*  
788 *for Numerical Methods in Engineering*, 54(11):1623–1648, 2002.
- 789 19. S Le Bras, H Deniau, and C Bogey. A flux reconstruction technique for non-conforming grid interfaces in  
790 aeroacoustic simulations. In *22nd AIAA/CEAS Aeroacoustics Conference, paper AIAA-2016-2972*, 2016.
- 791 20. L Cambier, S Heib, and S Plot. The Onera elsA CFD Software: Input from Research and Feedback from Industry.  
792 *Mechanics & Industry*, 14(03):159–174, 2013.
- 793 21. M Lazareff, AM Vuillot, and L Cambier. Manuel théorique du logiciel elsA, 2010.
- 794 22. D Fauconnier, C Bogey, and E Dick. On the performance of relaxation filtering for large-eddy simulation. *Journal*  
795 *of Turbulence*, 14(1):22–49, 2013.
- 796 23. F Kremer and C Bogey. Large-eddy simulation of turbulent channel flow using relaxation filtering: Resolution  
797 requirement and Reynolds number effects. *Computers & Fluids*, 116:17–28, 2015.
- 798 24. S Le Bras, H Deniau, C Bogey, and G Daviller. Development of compressible large-eddy simulations combining  
799 high-order schemes and wall modeling. *AIAA Journal*, pages 1–12, 2017.
- 800 25. EF Toro, M Spruce, and W Speares. Restoration of the contact surface in the HLL-Riemann solvers. *Shock waves*,  
801 4(1):25–34, 1994.
- 802 26. A Fosso Pouangué. *Schémas Volumes Finis Précis: application à l'aéroacoustique numérique de jets subsoniques*.  
803 PhD thesis, Université Pierre et Marie Curie, 2011.
- 804 27. DV Gaitonde and MR Visbal. High-order schemes for Navier-Stokes equations: algorithm and implementation into  
805 fdl3di. Technical report, DTIC Document, 1998.
- 806 28. H Wendland. *Scattered data approximation*, volume 17. Cambridge University Press, 2004.
- 807 29. MA Golberg, CS Chen, and H Bowman. Some recent results and proposals for the use of radial basis functions in  
808 the BEM. *Engineering Analysis with Boundary Elements*, 23(4):285–296, 1999.
- 809 30. JC Carr, RK Beatson, JB Cherrie, TJ Mitchell, WR Fright, BC McCallum, and TR Evans. Reconstruction and  
810 representation of 3D objects with radial basis functions. In *Proceedings of the 28th annual conference on Computer*  
811 *graphics and interactive techniques*, pages 67–76. ACM, 2001.
- 812 31. CKW Tam and JC Webb. Dispersion-relation-preserving finite difference schemes for computational acoustics.  
813 *Journal of Computational Physics*, 107(2):262–281, 1993.
- 814 32. G Fillola, MC Le Pape, and M Montagnac. Numerical simulations around wing control surfaces. *24th International*  
815 *Council of Aeronautical Sciences, paper ICAS-2004-2.3.2*, 2004.
- 816 33. C Bogey and C Bailly. Computation of a high Reynolds number jet and its radiated noise using large eddy  
817 simulation based on explicit filtering. *Computers & Fluids*, 35(10):1344–1358, 2006.
- 818 34. C Bogey, C Bailly, and D Juvé. Noise investigation of a high subsonic, moderate Reynolds number jet using a  
819 compressible large eddy simulations. *Theoretical and Computational Fluid Dynamics*, 16(4):273–297, 2003.
- 820 35. JC Lau, PJ Morris, and MJ Fisher. Measurements in subsonic and supersonic free jets using a laser velocimeter.  
821 *Journal of Fluid Mechanics*, 93(01):1–27, 1979.
- 822 36. C Bogey. Grid sensitivity of flow field and noise of high-Reynolds-number jets computed by large-eddy  
823 simulations. *International Journal of Aeroacoustics*, 17(4-5):399–424, 2018.
- 824 37. CKW Tam, K Viswanathan, KK Ahuja, and J Panda. The sources of jet noise: experimental evidence. *Journal of*  
825 *Fluid Mechanics*, 615:253–292, 2008.
- 826 38. Antares Development Team. Antares Documentation Release 1.11.0, 2012–2018.